A&A manuscript no.
(will be inserted by hand later)

Your thesaurus codes are:
08(02.19.1; 09.01.1; 09.09.1 Orion Peak 1; 09.13.2; 13.09.4)

ASTRONOMY AND ASTROPHYSICS

ISO-SWS Observations of OMC-1: H_2 and Fine Structure Lines⋆

Dirk Rosenthal[1], Frank Bertoldi[2], and Siegfried Drapatz[1]

[1] Max-Planck-Institut für extraterrestrische Physik, Giessenbachstrasse, D-85740 Garching, Germany, Rosenthal@MPE.MPG.de
[2] Max-Planck-Institut für Radioastronomie, Auf dem Hügel 69, D-53121 Bonn, Germany, Bertoldi@MPIfR-Bonn.MPG.de

Received ; accepted

Abstract. Using the Short-Wavelength-Spectrometer on the Infrared Space Observatory (ISO), we obtained near- and mid-infrared spectra toward the brightest H_2 emission peak of the Orion OMC-1 outflow. A wealth of emission and absorption features were detected, dominated by 56 H_2 ro-vibrational and pure rotational lines reaching from H_2 0–0 S(1) to 0-0 S(25). The spectra also show a number of H I recombination lines, atomic and ionic fine structure lines, and molecular lines of CO and H_2O. Between 6 and 12 μm the emission is dominated by PAH features.

The extinction toward the molecular and atomic line emitting regions is estimated from relative line intensities, and it is found that the H_2 emission arises from within the OMC-1 cloud at an average K-band extinction of 1.0 mag, whereas the atomic hydrogen emission and much of the fine structure emission comes from the foreground H II region and its bounding photodissociation front.

The total H_2 luminosity in the ISO-SWS aperture is estimated at (17 ± 5) $L_\odot$, and extrapolated to the entire outflow, (120 ± 60) $L_\odot$. The H_2 level column density distribution shows no signs of fluorescent excitation or a deviation from an ortho-to-para ratio of three. It shows an excitation temperature which increases from about 600 K for the lowest rotational and vibrational levels to about 3200 K at level energies $E(v, J)/k > 14\,000$ K. No single steady state shock model can reproduce the observed H_2 excitation. The higher energy H_2 levels may be excited either thermally in non-dissociative J-shocks, through non-thermal collisions between fast ions and molecules with H_2 in C-shocks, or they are pumped by newly formed H_2 molecules. The highest rotational levels may be populated by yet another mechanism, such as the gas phase formation of H_2 through H^-.

Key words: Shock waves – ISM: individual objects: Orion Peak 1 – ISM: molecules – Infrared: ISM: lines and bands

Send offprint requests to: D. Rosenthal

⋆ Based on observations with ISO, an ESA project with instruments funded by ESA Member States (especially the PI countries: France, Germany, The Netherlands, and the United Kingdom) and with the participation of ISAS and NASA.

1. Introduction

The Orion molecular cloud, OMC-1, located behind the Orion M42 Nebula at a distance of ∼450 pc (Genzel & Stutzki 1989), is the best-studied massive star forming region. This cloud embeds a spectacular outflow arising from some embedded young stellar object, which can possibly be identified as the radio source "I" 0.49 arcsec south of the infrared source IRc2-A (Menten & Reid 1995; Dougados et al. 1993). The outflow shocks the surrounding molecular gas, thereby giving rise to the strongest H_2 infrared line emission appearing in the sky (Fig. 1). Peak 1 (Beckwith et al. 1978) is the brighter of the two H_2 emission lobes of the outflow. Although the outflow has been studied extensively for nearly two decades, the nature of the excitation mechanism remains unclear.

Molecular hydrogen, through its infrared rotational and rotation-vibrational transitions, is an important coolant in shocks and photodissociation regions, and thereby a particularly well suited tracer of the flourescently- and/or shock-excited gas. The Short Wavelength Spectrometer (SWS, de Graauw et al. 1996) aboard the Infrared Space Observatory (ISO, Kessler et al. 1996) offered the first opportunity to observe pure rotational and rotation-vibrational H_2 lines from 2.4 μm to 28 μm with one instrument, unhindered by the Earth's atmosphere.

In this paper, we present a comprehensive set of intensities for 56 H_2 near- and mid-infrared lines we observed with the ISO-SWS. These observations trace populations of energy levels ranging from E/k =1015 K to 43 000 K. The redundancy of the H_2 level determinations provides information on the average gas excitation along the line of sight over an unprecedented range. This sheds new light on the possible excitation mechanisms in the IRc2 outflow.

We here concentrate on the interpretation of the H_2 and the atomic and ionic fine structure line emission, whereas a detailed discussion of the CO and H_2O lines will be presented in a separate paper (Boonman et al. 2000).

In a related paper we already discussed the detection of HD toward Orion Peak 1 (Bertoldi et al. 1999).

2. Observation

We observed OMC-1 in the SWS 01 ($2.4 - 45$ μm grating scan) and SWS 07 (Fabry-Pérot) modes of the short wavelength spectrometer (de Graauw et al. 1996) on board ISO on October 3, 1997, and in the SWS 02 ($\approx 0.01\lambda$ range grating scan) mode on September 20, 1997 and February 15, 1998. Fig. 1 illustrates the various aperture orientations with respect to the H_2 1-0 S(1) emission at 2.12 μm observed with NICMOS on the HST (Schultz et al. 1999).

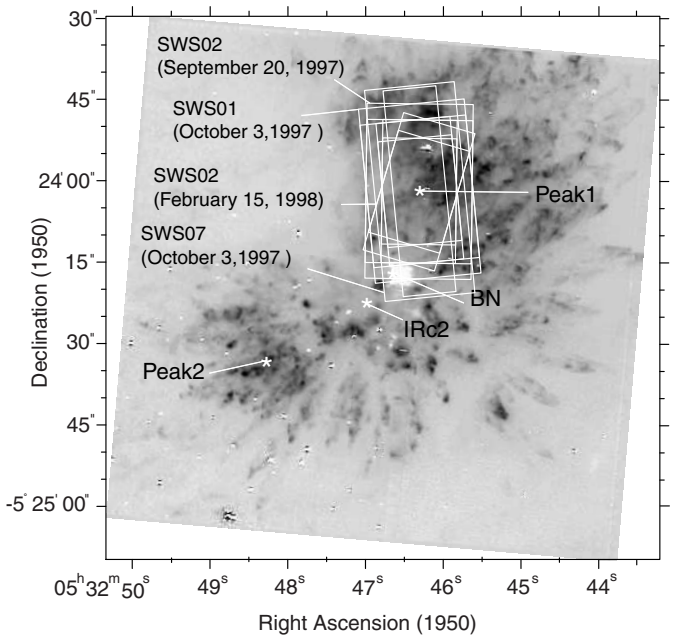

Fig. 1. H_2 1-0 S(1) emission of the OMC-1 outflow as seen with the NICMOS camera aboard the HST (Schultz et al. 1999). Overlaid are the various apertures of our ISO-SWS observations, which were centered on $\alpha_{2000.} = 5^{\rm h}35^{\rm m}13\overset{\rm s}{.}67$, $\delta_{2000.} = -5°22'8\overset{''}{.}5$, with an aperture of $14'' \times 20''$ for $\lambda < 12$ μm, $14'' \times 27''$ at 12 to 27.5μm, $20'' \times 27''$ at 27.5 to 29μm, and $20'' \times 33''$ at 29 to 45.2μm.

For the 2.4–45 μm spectrum of Peak 1 we used the slowest speed, highest spectral resolution full scan observing mode of the SWS. Data reduction was carried out using standard Off Line Processing (OLP) routines up to the Standard Processed Data (SPD) stage within the SWS Interactive Analysis (IA) system. Between the SPD and Auto Analysis Result (AAR) stages, a combination of standard OLP and in-house routines were used to extract the individual scans as well as for the removal of fringes. The flux calibration errors range from 5% at 2.4 μm to 30% at 45μm (SWS Instrument & Data Manual, Issue 1.0). The statistical uncertainties derived from the line's signal to noise ratio are for most detected lines smaller than the systematic errors due to flux calibration uncertainties.

3. Results and Discussion

Fig. 2 shows the full SWS 01 spectrum. Most of the observed continuum flux is probably coming from the strong Becklin Neugebauer (BN) source near the edge of the aperture. Aperture size changes from one band to another then cause changes in the intercepted continuum which are not simply proportional to the aperture size. In addition, there is extended continuum emission all over the outflow.

We normalized the line and continuum fluxes by the aperture size, assuming that there is uniform surface brightness at least for the line emission. The exact aperture profiles for the various wavelength bands is yet to be determined. Assuming an effective aperture resembling those shown in Fig. 1 is approximate. The error from this assumption, and the nonuniform continuum surface brightness cause additional relative offsets in the continuum fluxes of neighboring bands of –10% for the 7–12 μm band, -30% for the 12–16 μm band, +15% at 16–19.5 μm, -5% at 19.5–27.5 μm, -7.5% at 27.5–29.5 μm, and +5% above 29.5 μm.

Since the observed H_2 line intensities result in a smooth distribution of column densities in the excitation diagram, Fig. 8, the line intensities appear not to be affected much by the uncertainty of the aperture. Fig. 3 shows the SWS 01 spectrum in more detail. Fig. 4 shows selected lines at higher spectral resolution from line scan observation in the SWS 02 and SWS 07/SWS 06 modes. The SWS 06 grating spectra were simultaneously recorded with the SWS 07 Fabry-Perot spectra.

The Peak 1 spectrum is dominated by a large number of rotational and ro-vibrational H_2 lines. The pure rotational lines arise from levels with energies ranging from E/k =1015 K for the 0-0 S(1) line to E/k = 42 515 K for the 0-0 S(25) line. They represent gas with excitation temperatures ranging from 600 K for the low energy levels to over 3000 K for level energies $E/k > 14\,000$ K. The observed fluxes of the identified H_2 lines are listed in Table 3. The spectrum is rich also in H I recombination lines and atomic and ionic fine structure lines. Between 4.5 to 5 μm, we find a forest of gaseous 1-0 ro-vibrational CO emission, possibly mixed with absorption of solid CO (van Dishoeck et al. 1998). Gaseous water is seen in emission through the ν_2 bending mode between 6.3 and 7 μm and several lines between 30 and 45 μm, and gaseous CO_2 is detected at 15 μm. PAH features dominate the emission between 6 and 12 μm. Absorption features of water ice are seen at 3.1 μm, of CO_2 ice at 4.25 μm, and of silicate at 9.7 μm.

The various observed lines and features probe different regions – both within the SWS aperture and along the line of sight. The H II region in the foreground of OMC-1 contributes to the H recombination and ionic fine struc-

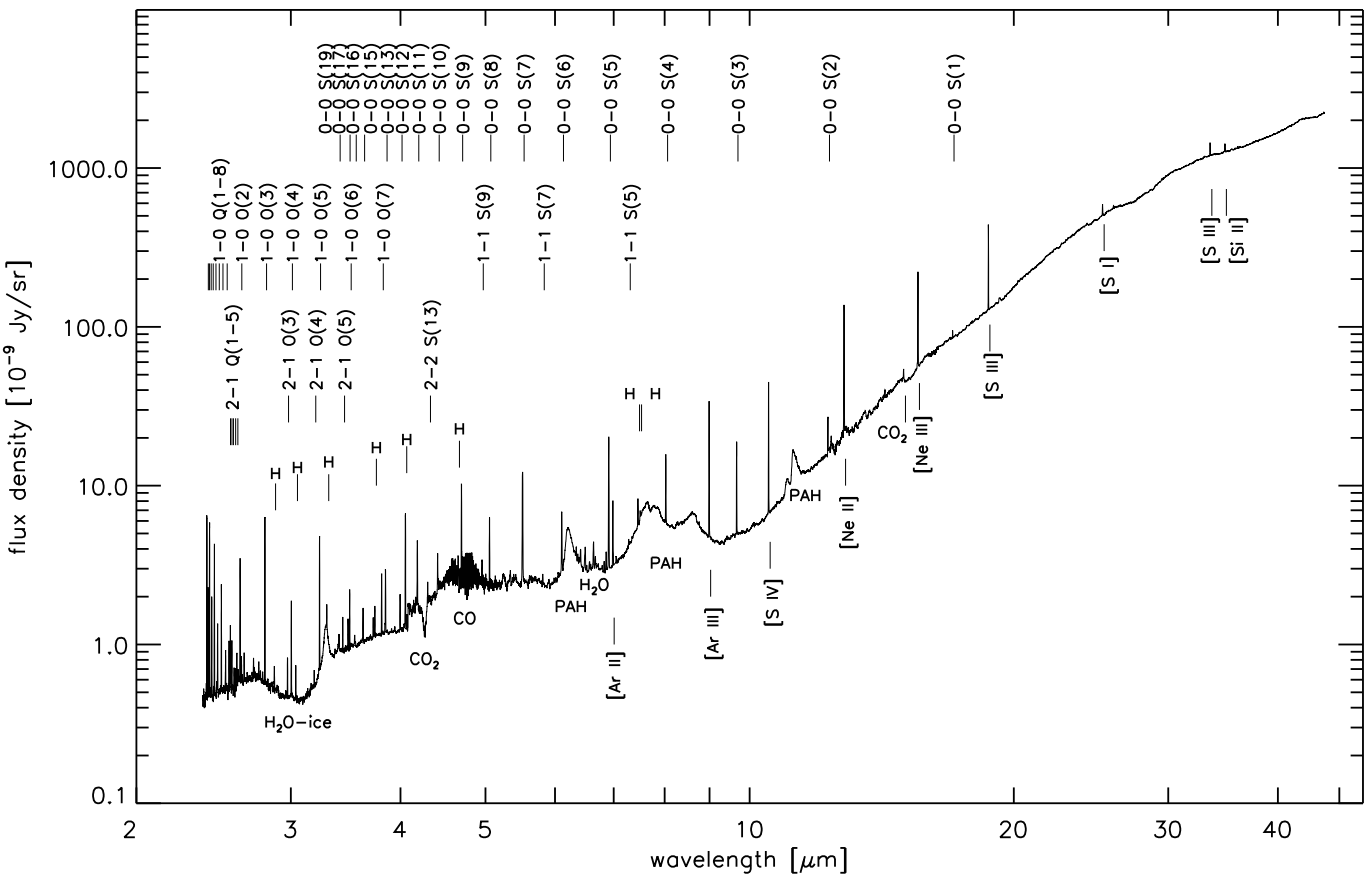
flux density [10^{-9} Jy/sr]
wavelength [μm]
1000.0
100.0
10.0
1.0
0.1
2
3
4
5
10
20
30
40
0–0 S(19)
0–0 S(17)
0–0 S(16)
0–0 S(15)
0–0 S(13)
0–0 S(12)
0–0 S(11)
0–0 S(10)
0–0 S(9)
0–0 S(8)
0–0 S(7)
0–0 S(6)
0–0 S(5)
0–0 S(4)
0–0 S(3)
0–0 S(2)
0–0 S(1)
1–0 Q(1–8)
1–0 O(2)
1–0 O(3)
1–0 O(4)
1–0 O(5)
1–0 O(6)
1–0 O(7)
1–1 S(9)
1–1 S(7)
1–1 S(5)
2–1 Q(1–5)
2–1 O(3)
2–1 O(4)
2–1 O(5)
2–2 S(13)
H
H
H

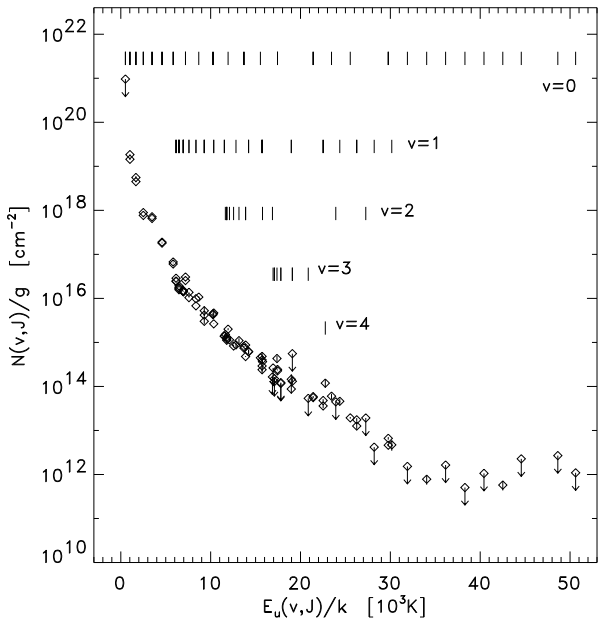

Fig. 5. Excitation diagram of the H_2 level column density distribution toward Peak 1, plotting the observed level columns (not corrected for extinction, divided by the level degeneracy) against level energy.

the smooth line-up we observed here, where N/g appears not to depend on the state quantum number. Furthermore, fluorescently excited gas usually shows ortho-to-para ratios in vibrationally excited levels smaller than the total ortho-to-para ratio of the gas along the line of sight. This is due to the enhanced self-shielding, and therefore reduced excitation rate, of the more abundant ortho-H_2 (Sternberg & Neufeld 1999).

3.2. Extinction

The shocks emitting the strong infrared lines in the OMC-1 outflow are deeply embedded in the molecular cloud, so that the emerging radiation suffers significant extinction. To correct the column densities derived from the H_2 emission line intensities, $N_{\rm obs}(v, J)$, for this extinction, we need to know the proper extinction correction as a function of wavelength. However, this interstellar infrared extinction curve is not well determined. Especially the depth and width of the silicate absorption features, centered at 9.7 μm and 18 μm are uncertain, and they could vary from region to region (Draine 1989). A further complication arises from the mixing of the emitting and absorbing gas, which we might expect in the outflow regions considering the complex spatial variation of the near-IR emission mapped in OMC-1 (Fig. 1), or in similar outflows such as DR21 and Cep A (Davis & Smith 1996; Goetz et al. 1998).

With enough redundancy in the information provided by the molecular and atomic lines in Peak 1, we are in principle able to estimate the average extinction along our line of sight as a function of wavelength. However, the H I recombination lines and the H_2 emission lines may not be tracing the same regions, and might therefore be subject to differing extinction. We therefore treat them separately. To correct the H_2 line fluxes for extinction, we tried to derive the extinction from the H_2 lines directly (Bertoldi et al. 1999).

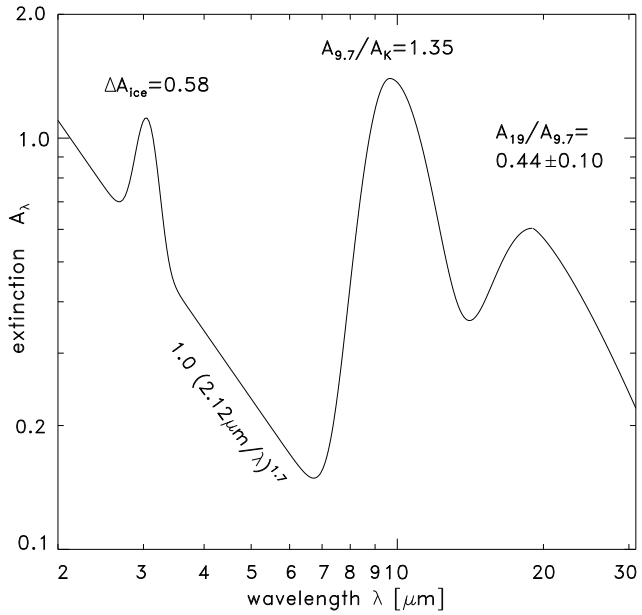

Fig. 6. Near- and mid-infrared extinction (Eq. 2) found from the relative intensities of the H_2 lines observed toward Peak 1. The curve was constructed using four free parameters for which values were derived that minimize the dispersion of the H_2 column density distribution (Fig. 5) for levels with $E/k < 16\,000$ K

An inspection of the excitation diagram Fig. 5 derived from the line intensities (*uncorrected* for extinction) shows that the column densities follow a smooth distribution, with no dependence on vibrational quantum number, and no sign of an ortho-to-para column density ratio different from three. Transitions from a given state to different lower states produce lines with different wavelengths which suffer extinction. Deviations from the expected line ratios of lines from the same state therefore yield the difference in extinction between the corresponding wavelengths of the lines. More generally, we can use this to estimate the extinction as a function of wavelength for a large set of lines, by minimizing the dispersion in the excitation diagram around a least-squares fit to the level

columns. We thereby assume that the dispersion in the column densities is partly due to extinction.

We constructed an extinction curve (Fig. 6) with four free parameters: the absolute normalization for a $A_\lambda \propto \lambda^{-1.7}$ power law extinction curve from 2.4 μm to 6 μm, the width and depth of the water ice absorption feature at 3.1 μm, and the depth of the 9.7 μm silicate absorption feature. We fixed the width of the 9.7 and 18 μm silicate features from calculations by Draine & Lee (1984). The depth of the 18 μm feature was taken to be 0.44 times that of the 9.7 μm feature, based on an average of previous estimates (Draine & Lee 1984; Pegourie & Papoular 1985; Volk & Kwok 1988; Bertoldi et al. in prep.). Calibration uncertainties and a small contribution of foreground fluorescently excited H_2 may give rise to a dispersion in the derived extinction corrections that is not due to extinction. The derived curve should therefore be considered as very approximate. The extinction curve minimizing the dispersion in the excitation curve is shown in Fig. 6. Explicitly it can be written

$$\begin{aligned} A(\lambda) \;=\; & A_{\rm K}(\lambda/2.12)^{-1.7} + 0.58\; e^{-22(\lambda-3.05)^2} \\ & + (1.35 - 0.08 A_{\rm K}) \left\{ e^{-[c_1 \log(\lambda/9.66)]^2} \right. \\ & \left. + 0.44\; e^{-[c_2 \log(\lambda/19)]^2} \right\} \;, \end{aligned} \qquad (2)$$

where $A_{\rm K} = (1.0 \pm 0.1)$ mag is the implied extinction at 2.12 μm, and $c_1 = 14.3$ for $\lambda < 9.7$, $c_1 = 9.8$ for $\lambda > 9.7$, $c_2 = 7.5$ for $\lambda < 19$, $c_2 = 4.8$ for $\lambda > 19$, and λ is given here in μm. The depth of the extinction minimum at 6.5 μm is very uncertain, since it is not constrained by the inconsistent corrections derived from the four lines between 5.8 and 7.3 μm. There is an indication that the minimum is at least as deep as our simple curve shows, but a much more careful analysis of the line fluxes would be necessary to reach a firm conclusion.

Atomic hydrogen recombination lines could offer another means to trace the extinction as a function of wavelength. We detected seventeen H I recombination lines ranging in wavelength from 2.6 to 19 μm. Since the relative emissivities are known from theory (Storey & Hummer 1995) and depend only mildly on the gas temperature and density, a comparison of the observed line intensities divided by their respective case B emissivities yields a measure for the differential extinction between the respective lines' wavelengths.

In Fig. 7 we plot against wavelength the observed line intensities, divided by their emissivities and normalized to this ratio for the H I 8–5 transition line. The data points scatter around unity, which means that there is little if any differential extinction over this wavelength range. A comparison with the distribution of intensities expected for an extinction curve with the shape we found from the H_2 lines reveals none of the prominent extinction features. A reasonable explanation is that the total extinction to the H I emission region is very low, $A_{\rm K} < 0.3$ mag.

Although the errors are too large to constrain the exact value of the extinction, it is obvious that the H recombination lines are much less attenuated than the H_2 lines. This suggests that the bulk of the atomic hydrogen emission arises in the foreground H II region, whereas the H_2 emitting region is more deeply embedded in the molecular cloud.

This conclusion agrees with the assessment of Everett et al. (1995), who obtained $A_{\rm J} = (0.38 \pm 0.09)$ mag for the extinction shown by H recombination lines, but found $A_{\rm J} = (2.15 \pm 0.26)$ mag from the H_2 lines. With a $\lambda^{-1.7}$ extinction law this corresponds to $A_{\rm K} = (0.15 \pm 0.04)$ mag and $A_{\rm K} = (0.9 \pm 0.1)$ mag, in good agreement with our results.

3.3. Fine structure lines

The observed atomic and ionic fine structure lines are valuable diagnostics. If highly-ionized species are found toward the shocked region – which is well shielded from the ionizing radiation of the Trapezium stars – they would indicate the presence of fast, ionizing J-shocks. It is therefore interesting to disentangle the respective contributions to the fine structure line emission of the foreground H II region/PDR and the shocked gas of the OMC-1 outflow.

Table 1 lists the observed intensities of a number of fine structure lines we searched for toward Peak 1.

A predominantly ionized medium is traced by species with ionization potentials larger than 13.6 eV. From such ions a number of lines, [Ar II]6.9μm, [Ar II]8.99μm, [Ne II]12.8μm, [Ne III]15.5μm, [Ne III]36μm, [S III]18.7μm, and [S IV]10.5μm, are found in our ISO-SWS spectra, and their intensities can be compared with H II region models such as those computed by Rubin et al. (1991). A comparison of the line intensities and their ratios to a blister H II region model with a star of $T_{\rm eff} = 37\,000$ K and $\log g = 4.0$, shows good agreement of all line intensities, except for that the models overestimate the [S III]18.7μm/[S III]33.5μm ratio by a factor 1.8. The good agreement indicates that these lines may be predominantly produced in the foreground H II region, although a shock contribution of up to 30% cannot be excluded.

We can compare the Peak 1 fine structure line emission also with that seen toward the Orion Bar photodissociation region and ionization front, which is also irradiated by the Trapezium stars. We know that here no fast shocks should contribute to the emission, and that the emission should be similar to that coming from the PDR in front of the OMC-1 outflow (Herrmann et al. 1997). In Table 2 we list line intensities we observed toward two positions on the Orion Bar: toward the ionization front at $5^{\rm h}35^{\rm m}19.31^{\rm s}$, $-5°24'59.9''$ (J2000), and toward the peak of the H_2 1-0 S(1) emission at $5^{\rm h}35^{\rm m}20.31^{\rm s}$, $-5°25'19.9''$. A comparison with the Peak 1 intensities shows that the intensities of most lines agree within a factor of a few, suggesting that ionic emission indeed arises in the foreground H II region.

Table 1. ISO-SWS Observations of Fine Structure Lines toward Orion Peak 1

	λ [μm]	IP_l [a] [eV]	IP_u [b] [eV]	n_{crit} [c] [cm^{-3}]	SWS AOT	I_{obs} [erg s^{-1}cm^{-2}sr^{-1}]	S/N [d]	A_λ [e] [mag]	I_{model} [f] [erg s^{-1}cm^{-2}sr^{-1}]
[Ne III]	36.009	40.96	63.45	5.52×10^4	01	2.26×10^{-3}	4.3	0.02	1.78×10^{-3}
[Fe II]	35.777	7.90	16.19		01	1.22×10^{-3}	2.0	0.02	
[Si II]	34.814	8.15	16.35	3.67×10^5 [g]	01	1.43×10^{-2}	19.1	0.03	3.16×10^{-4}
					02	1.59×10^{-2}	58.8		
[S III]	33.480	22.34	34.79	6.34×10^3	01	2.16×10^{-2}	46.0	0.03	1.20×10^{-2} [h]
[Fe II]	25.988	7.90	16.19	3.59×10^4 [i]	01	3.70×10^{-3}	6.8	0.05	
					02	1.76×10^{-3}	10.6		
[S I]	25.249	0.0	10.36	4.2×10^4 [j]	01	1.19×10^{-2}	19.5	0.35 [k]	
					02	1.17×10^{-2}	20.5		
[Fe III]	22.925	16.19	30.65	1.12×10^5	01	4.15×10^{-4}	2.1	0.07	
[S III]	18.713	23.34	34.79	2.06×10^4	01	3.61×10^{-2}	307.0	0.09	3.63×10^{-2}
[Fe II]	17.936	7.90	16.19		01	2.56×10^{-4}	2.2	0.09	
[P III]	17.885	19.77	30.20	3.91×10^4	01	3.09×10^{-4}	2.9	0.09	
[Ne III]	15.555	40.96	63.45	2.70×10^5	01	3.20×10^{-2}	255.0	0.07	2.80×10^{-2}
[Ne II]	12.814	21.56	40.96	6.54×10^5	01	3.03×10^{-2}	109.0	0.07	3.16×10^{-2}
					02	3.11×10^{-2}	63.3		
[S IV][l]	10.511	34.79	47.22	5.39×10^4	01	9.69×10^{-3}	550.0	0.19	2.40×10^{-2}
[Ar III]	8.991	27.63	40.74	3.18×10^5	01	9.29×10^{-3}	323.0	0.18	1.38×10^{-2}
[Ar II]	6.985	15.76	27.63	4.17×10^5	01	2.92×10^{-3}	148.0	0.02	2.82×10^{-3}
[Ni II][m]	6.636	7.64	18.17	1.73×10^7	01	1.26×10^{-3}	47.8	0.02	

[a] Lower ionization potential, IP_l, to produce the ion.
[b] Upper ionization potential, IP_u, of the next higher ionization stage.
[c] Collisions with electrons at $T = 10\,000$ K, unless indicated.
[d] Calculated from the RMS noise within $\sim 500\,\mathrm{km\,s^{-1}}$.
[e] From the extinction law of Bertoldi et al. (1999) with A_K =0.15 mag.
[f] Best model by Rubin et al. (1991) for a projected distance of $\sim 86''$ from θ^1 Ori C.
[g] For collisions with electrons at 20 000 K. Collisions with H atoms at 300 K yield $n_{crit} = 3.67 \times 10^5$ cm^{-3}.
[h] From the predicted [S III]18.7μm line intensity and the [S III]18.7μm/[S III]33.5μm line ratio.
[i] Collisions with H atoms yield $n_{crit} = 2.24 \times 10^6$ cm^{-3}.
[j] For collisions with H^+ ions. Collisions with H atoms at 300 K yield $n_{crit} = 1.5 \times 10^6$ cm^{-3}.
[k] Because [S I]25.249μm probably arises from the more deeply embedded, shocked region, we adopt $A_K = 1.0$ as for the H_2 emission, with the extinction curve of Fig. 6.
[l] Merged with H 12-8, but we estimate latter to contribute only 4×10^{-5} erg s^{-1}cm^{-2}sr^{-1}, adopting case-B emissivities.
[m] Merged with an H_2O line at 6.6354 μm.

The [P III]17.9μm, [Fe III]22.9μm, [Fe II]26μm, and the [S III]33.5μm lines were not included in the Rubin models, but their intensities are very similar toward the outflow and the Bar. It is unclear where the [Fe II]26μm emission comes from, though. It could be produced either in the PDR or in the ionization front. A detailed analysis of the [Fe II] emission will be subject of a subsequent publication (Bertoldi et al., in prep.).

Silicon: Haas et al. (1991) observed [Si II]34.8μm strip maps across the OMC-1 outflow. From the apparent peak of emission near IRc2 they concluded that about half of this emission must be due to the production and excitation of gas phase silicon in shocks. In their preliminary reduction of a $\sim 6'$ square map of [Si II], Stacey et al. (1995) also find that the emission peaks toward the OMC-1 outflow, and this excess is consistent with that observed by Haas et al. (1991). Haas et al. find a surface flux density of 6×10^{-3} erg cm^{-2}s^{-1}sr^{-1} toward Peak 1, of which they attribute about half to an extended component, which most likely arises from the PDR lining the foreground H II region. Haas et al. find that the flux is similar toward Peak 1 and the Orion Bar, which may well be due to limb brightening by a factor two of the PDR component at the Bar. Our observations of [Si II]34.8μm toward the Bar and Peak 1 yield fluxes twice as high as those of Haas. This could be due either to a calibration error, or to beam dilution in the Haas et al. measurements. Either way, it seems that both the PDR and the shocks give rise to strong silicon emission, which for the PDR at least requires Si gas phase abundances of order 10% solar: the PDR models by Tielens & Hollenbach (1985b) adopt a 2.2% solar gas phase Si abundance and predict about a quarter of the flux we could attribute to the PDR. The silicon abundance can

Table 2. Fine Structure Lines toward two Positions on the Orion Bar PDR

		Bar H_2 S(1)				Bar Brγ			
	λ [μm]	SWS AOT	I_{obs} [erg s^{-1}cm^{-2}sr^{-1}]	S/N [a]	Bar/Pk1 [b]	SWS AOT	I_{obs} [erg s^{-1}cm^{-2}sr^{-1}]	S/N	Bar/Pk1 [b]
[Ne III]	36.009	01	1.75×10^{-3}	12.9	0.8	01	1.31×10^{-3}	1.8	0.6
[Fe II]	35.777	01	2.05×10^{-4}	2.8	0.2				
[Si II]	34.814	01	1.38×10^{-2}	135.0	1.1	01	1.16×10^{-2}	7.1	1.0
						02	1.13×10^{-2}	63.7	0.7
[S III]	33.480	01	2.70×10^{-2}	88.4	1.3	01	4.78×10^{-2}	36.4	2.2
[Fe II]	25.988	01	1.38×10^{-3}	19.4	0.4	01	9.58×10^{-4}	4.2	0.3
						02	1.37×10^{-3}	17.8	0.8
[S I][d]	25.249	01	$< 1.9 \times 10^{-4}$		< 0.02	01	$< 2.1 \times 10^{-4}$		< 0.02
[Fe III]	22.925	01	4.82×10^{-4}	10.6	1.2	01	1.64×10^{-3}	4.4	4.0
						02	9.60×10^{-4}	15.6	2.3
[Ar III]	21.842	01	3.59×10^{-4}	6.0					
[S III]	18.713	01	2.08×10^{-2}	391.0	0.6	01	5.19×10^{-2}	249.0	1.4
[Fe II]	17.936	01	4.22×10^{-5}	2.1	0.1				
[P III]	17.885	01	1.56×10^{-4}	6.6	0.5				
[Ne III]	15.555	01	7.54×10^{-3}	186.0	0.2	01	2.62×10^{-2}	575.0	0.8
[Ne II]	12.814	01	1.49×10^{-2}	76.5	0.5	01	3.44×10^{-2}	70.6	1.1
[S IV][c]	10.511	01	2.29×10^{-3}	100.0	0.2	01	8.38×10^{-3}	55.0	0.9
[Ar III]	8.991	01	3.69×10^{-3}	116.0	0.4	01	1.13×10^{-2}	194.0	1.2
[Ar II]	6.985	01	1.90×10^{-3}	18.7	0.7	01	1.15×10^{-2}	40.2	3.9
[Ni II][d]	6.636	01	$< 7.7 \times 10^{-5}$		< 0.06	01	$< 1.4 \times 10^{-4}$		< 0.1

[a] From the RMS noise within $\sim 500\,\mathrm{km\,s^{-1}}$.
[b] Ratio of the respective intensities toward Bar H_2 S(1) and Peak 1, and Bar Brγ and Peak 1. If lines in different observing modes are available the ratio was calculated from lines of the same mode.
[c] The [S IV] line is merged with the H 12-8 line.
[d] The upper limit for the intensities is calculated from the 3σ flux density noise level at the respective wavelength times the width of one resolution element.

be enhanced in shocks by sputtering (Martin-Pintado et al. 1992; Caselli et al. 1997; Bachiller & Perez-Gutierrez 1997). Large gas phase silicon abundances are also found in other PDRs such as NGC 7023 (Fuente et al. 1999). The mechanism by which the abundance is enhanced in PDRs is still unclear, although photodesorption has been suggested (Walmsley et al. 1999). Strong silicate emission is however not a universal feature of PDRs: based on ISO observations of [Si II]34.8μm toward NGC 2023 and a comparison with model calculations, Draine & Bertoldi (2000) report Si to be quite highly depleted in the NGC 2023 PDR.

Other lines: Of the other fine structure lines seen toward Peak 1, [Ni II]6.6μm and [S I]25μm are not detected toward the Orion Bar. The [Ni II]6.6μm line is confused with a water line, making it difficult to detect. Although the [Fe II]18μm and [Fe II]36μm lines are marginally detected in both objects, they both appear to be an order of magnitude fainter toward the Bar than toward Peak 1. This suggests that shocks are more efficient in producing and exciting gas phase iron.

Sulfur: The strong [S I]25μm line emission is probably shock-excited. Burton et al. (1990a) computed the [S I] intensity in their PDR model for densities of 10^3 to $10^5\,\mathrm{cm^{-3}}$ and radiation fields of 10^3 to 10^5 times the ambient interstellar field as $\leq 10^{-5}\,\mathrm{erg\,s^{-1}\,cm^{-2}\,sr^{-1}}$, which is three orders of magnitude below our observed [S I] intensity. Both a J- or C-type shock could account for the [S I] emission. But only a J-shock is able to produce both the [S I] and the [Si II] line emission.

We compared the estimated shock contribution to the observed [Si II]34.8μm flux of $\sim 7\times10^{-3}\,\mathrm{erg\,s^{-1}\,cm^{-2}\,sr^{-1}}$ (Haas et al. 1991) and the [S I]25μm line flux to the J-shock model of Hollenbach & McKee (1989). Both the relative and absolute [S I] and [Si II] fluxes could be explained by shocks of high velocities, $v_s = (85 \pm 10)\,\mathrm{km\,s^{-1}}$, a pre-shock hydrogen nuclei density $n_H = (10^5 - 10^6)\,\mathrm{cm^{-3}}$, and a beam filling factor $\phi \sim 3 - 4$. A beam-filling planar shock results in $\phi = 1$, and a beam-filling spherical shock in $\phi = 4$. A shock contribution of 10 to 30% to the [Ne II]12.8μm flux would also explain the observed [Ne II]/[Si II] and [Ne II]/[S I] flux ratios.

3.4. Molecular hydrogen

In the spectra shown in Figs. 2, 3, and 4, we detected 56 different H_2 lines of pure rotational and rotation-vibrational transitions (Table 3). Pure rotational lines were detected ranging from the 0-0 S(1) to 0-0 S(25) transitions, which correspond to upper level energies $E(v,J)/k$ ranging from 1015 K to 42 500 K. Adding a large number of vibration-rotational transition lines, we are able to study the excitation of the gas within the ISO aperture over an unprecedented range.

The H_2 0-0 S(0) transition line was not detected from our observations with the medium resolution grating modes (SWS 01 and SWS 02, $R \sim 1000 - 2000$). Unfortunately, our observation with the Fabry-Perot did not cover a spectral range wide enough to detect a line with the expected width of ~ 60 km s^{-1} (Nadeau & Geballe 1979; Brand et al. 1989b, Moorhouse et al. 1990; Chrysostomou et al. 1997). However, the FP spectrum, shown in Fig. 4, shows a line-like feature with a a narrow width of 12 km s^{-1}, comparable to the spectral resolution in this observing mode. This feature could be emission arising in the foreground photodissociation region bounding the Orion Nebula and the dense molecular cloud embedding the outflow.

3.4.1. Contribution from the foreground PDR

The line emission toward Peak 1 must include some contribution from the photodissociation region bordering the foreground Orion Nebula H II region. Garden (1986) produced a H_2 1-0 S(1) map which covers OMC-1, the Trapezium, and the Orion Bar PDR. Following Burton & Puxley (1990b), we estimate that the extended fluorescent H_2 flux should amount to about 5% of the total H_2 emission toward Peak 1 over the SWS aperture.

For an additional estimate of the expected PDR contribution we can compare the total H_2 luminosity toward Peak 1 to that toward the Orion Bar, a PDR observed nearly edge-on south-east of the Trapezium. We did observe the Bar with the ISO-SWS (Bertoldi et al., in prep.), and find that the total H_2 emission here amounts to 0.008 erg s^{-1}cm^{-2}sr^{-1}, compared to the 0.28 erg s^{-1}cm^{-2}sr^{-1} toward Peak 1. Since the Bar is the brightest PDR emission peak in the Orion Nebula, we see that the H_2 emission from the PDR toward Peak 1 is probably small compared with the emission arising from the deeply embedded outflow.

3.4.2. Excitation of molecular hydrogen

From the line intensities we derived observed column densities of the levels from which these transitions arise (Eq.1). We correct these values for extinction with the curve we derived in Sec. 3.2 (Fig. 6), to obtain the inherent level column densities

$$N(v,J) = N_{\rm obs}(v,J) \;\; 10^{0.4A(\lambda)}. \tag{3}$$

The resulting excitation (Boltzmann) diagram is shown in Fig. 8.

The lack of signs of fluorescent excitation in the level columns suggest that the molecules might be mostly thermally excited. An H_2 column $N_{\rm H_2,tot}$ in statistical (thermodynamic) equilibrium at a single kinetic temperature T would yield a level distribution

$$\frac{N(v,J)}{g_J} \;=\; N_{\rm H_2,tot}\,\frac{e^{-E(v,J)/kT}}{\sum_{v',J'} g_{J'}\, e^{-E(v',J')/kT}}, \tag{4}$$

which produces a straight line in the Boltzmann (excitation) diagram Fig. 8. An excitation temperature function, $T_{\rm ex}(E)$, can be assigned to the level distributions at each level energy, $E(v,J)$, by computing the inverse of the derivative of the line which best fits $\ln[N(v,J)/g_J]$ as a function of $E(v,J)/k$. Near the lowest energy levels, $T_{\rm ex} \sim 600$ K, whereas at $E(v,J)/k \geq 14\,000$ K, the excitation temperature rises to ~ 3200 K.

To describe the range of excitation temperatures, we decomposed the distribution of column densities to a sum of five Boltzmann distributions of different excitation temperatures:

$$N(v,J)/g_J = \sum_{i=1}^{5} C_i\; e^{-E(v,J)/kT_{{\rm ex},i}}, \tag{5}$$

where we chose $T_{{\rm ex},i} = (628, 800, 1200, 1800, 3226)$ K, and the C_i (see Table 4) were determined by a least-squares-fit to the observed level columns. In Fig. 8 the dotted line shows the five-component fit. From this fit we can also compute the total warm H_2 column density, by summing the column densities over *all* levels following the interpolated level column distribution:

$$\begin{aligned} N_{\rm H_2,tot} \;&=\; \sum_{v,J}\left[\frac{N(v,J)}{g_J}\right] g_J \\ &=\; \sum_{v,J}\sum_{i=1}^{5} g_J\, C_i\; e^{-E(v,J)/kT_{{\rm ex},i}} \\ &=\; (1.9 \pm 0.5) \times 10^{21}\ {\rm cm}^{-2}. \end{aligned} \tag{6}$$

Adopting a distance of 450 pc (Genzel & Stutzki 1989), this column corresponds to a warm H_2 mass of (0.06 ± 0.015) $M_\odot$ within the ISO-SWS aperture.

By summing from $J = 0$, we extrapolated the observed H_2 ($v = 0, J \geq 3$) level populations to the unobserved ($v = 0, J = 0, 1, 2$) levels. Note that thereby we estimate the total *warm* H_2 column density, but we do not account for the *total* H_2 column along the line of sight, which includes an additional $\approx 10^{22}$ cm^{-2} cold gas from the molecular cloud which embeds the outflow. Most of this cold H_2 resides in the ground states $J = 0$ and $J = 1$, and does

Table 4.

$T_{ex,i}$ (K)	C_i (cm^{-2})	$N_{H_2,i}$ (cm^{-2})	fraction of warm H_2
628	8.80×10^{19}	1.37×10^{21}	72.2%
800	2.01×10^{19}	3.96×10^{20}	20.9%
1200	3.62×10^{18}	1.07×10^{20}	5.7%
1800	3.83×10^{17}	1.76×10^{19}	0.9%
3226	7.01×10^{16}	6.82×10^{18}	0.4%

not contribute to the emission observed from the shock-excited gas in the outflow.

By changing the order of summation in Eq. 6 we can compute the column densities corresponding to the five excitation temperature components, $N_{H_2,i}$ (Table 4), such that

$$N_{H_2,tot} = \sum_{i=1}^{5} \sum_{v,J} g(J)\, C_i\, e^{-E(v,J)/k\,T_{ex,i}} = \sum_{i=1}^{5} N_{H_2,i}. \quad (7)$$

Figure 9 shows the corresponding cummulative column density, $N_{H_2}(T_{ex} > T)$, plotted against T. With the interpolated excitation distribution Eq. 5 the column densities of all H_2 energy levels can be estimated, even those from which no lines were observed. Then the total H_2 rovibrational emission from the electronic ground state extrapolates to (0.28 ± 0.08) erg $s^{-1}cm^{-2}sr^{-1}$. Over the ISO-SWS aperture this amounts to (17 ± 5) $L_\odot$. Compared with the total observed H_2 line emission (after extinction correction) of (0.16 ± 0.05) erg $s^{-1}cm^{-2}sr^{-1}$, we find that our line spectra account for more than half of the total H_2 emission.

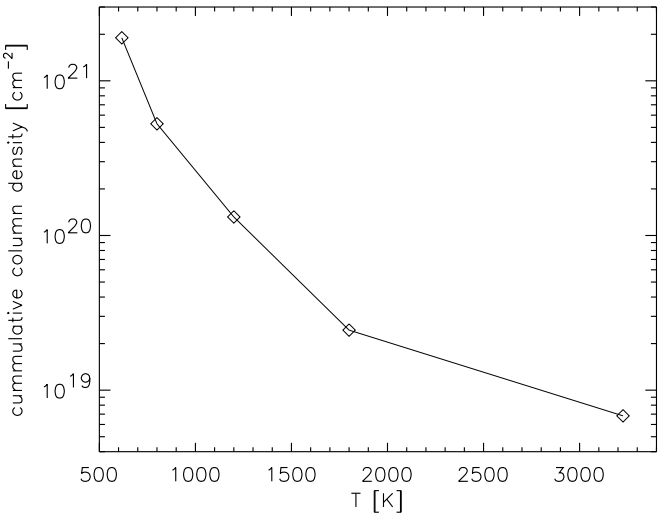

Fig. 9. Cummulative column density of H_2 with excitation temperatures larger than a given value of T, observed within the ISO aperture. Derived from the five-component decomposition listed in Table 4.

Our observations target the brightest field in the Orion outflow. The outflow covers an area of about $2' \times 2'$. The average H_2 brightness over this area we estimate from the 1-0 S(1) map of Garden (1986) to approximately 20% of that in our observed field, so that the total H_2 luminosity of the OMC-1 outflow is estimated to be (120 ± 60) $L_\odot$. This is consistent with the 94 $L_\odot$ estimated by Burton & Puxley (1990b).

3.4.3. What excites the highest-energy levels?

Table 4 and Fig. 9 illustrate that only a small fraction of the warm molecular gas is at the high excitation temperatures, which reach 3000 K. This is difficult to reconcile with the expected smooth temperature profile of a single planar C-type shock, in which the gas temperature changes smoothly, and where a large fraction of the warm gas is near the maximum temperature (Timmermann 1996b). Even with a distribution of shock speeds, and a correspondingly wide range in peak temperatures, an excitation temperature distribution similar to that shown in Fig. 9 is difficult to understand. It would require a velocity distribution where only a small fraction, about 1%, of the gas is shocked at the high speed necessary to produce a 3000 K excitation. In bow shocks, e.g., the velocity changes slowly with distance from the apex, and such a distribution of velocities would not be expected.

In dissociative J-type shocks, the molecules are destroyed in the shock, and they reform in a postshock layer where the temperature has dropped much below 3000 K, somewhat dependent on the H_2 formation rate efficiency at higher temperatures, which is essentially unknown (e.g. Bertoldi 1997). Dissociative J-shocks can therefore not account for the high excitation H_2 we observe.

Even if temperatures of 3000 K or more can be reached in non-dissociative shocks, the higher H_2 levels would remain subthermally excited unless the gas density is high enough that the collisional excitation and deexcitation rates are comparable to those for radiative decay. A "critical" gas density can be defined for a given level as that for which the total collisional deexcitation rate of this level equals its total radiative decay rate. In Fig. 10 we plot the critical density computed this way for states in the vibrational ground state, $v = 0$, up to $J = 16$. We see that even at kinetic temperatures of 3000 K, gas densities above $10^6 cm^{-3}$ would be necessary to maintain the high $v = 0$ levels at populations resembling LTE. Since such high densities may not prevail in the shocked gas of the Orion outflow, we may explore mechanisms other than thermal excitation that could account for the population of the higher energy states (see also Bertoldi et al. 2000).

Time-dependent C-shocks: When a high velocity outflow strikes dense molecular gas and thereby a C-type shock is first established, J-type shocks can temporarily form

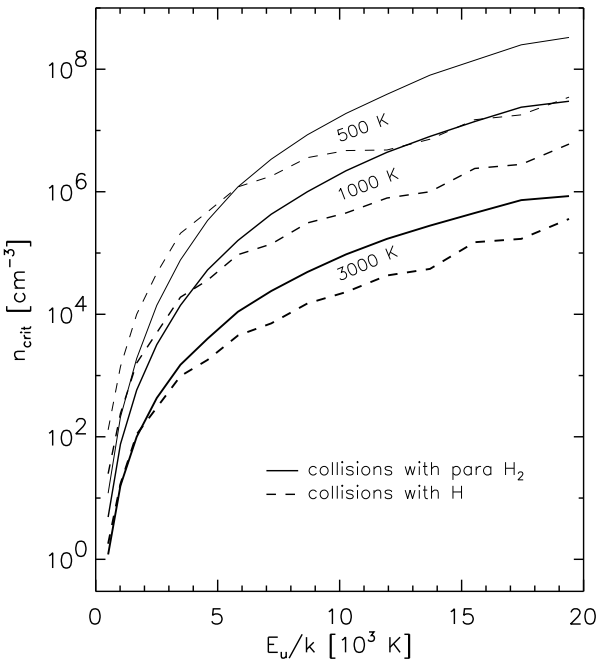

Fig. 10. Critical densities, $n_{\rm crit}$, of $v = 0$ states of H_2 as a function of level energy, for H_2–H_2 and H_2–H collisions. The critical density is the ratio between the sum of all radiative rate (Einstein-A) coefficients, and the sum of the collisional deexcitation rate coefficients from a state to all states with lower energy. Einstein-A coefficients were adopted from Turner et al. (1977), and collisional rate coefficients from Bourlot et al. (1999).

within the C-shock. In such an embedded J-shock, a small column of gas is heated to high temperatures (Chièze et al. 1998), and if the density is sufficiently high, this could account for the high-excitation tail of the column density distribution (Flower & Pineau des Forêts 1999). The lifetime of the embedded J-shock is small, so that the high-temperature excitation tail would be a transient phenomenon, unless shocks are constantly reforming. Embedded J-shocks may also form when a C-shock encounters dense clumps.

Formation pumping: Another possible pumping mechanism of the high-energy states is the formation of H_2. Molecular hydrogen is believed to form on the surfaces of dust grains. Some of the 4.5 eV released during the formation of an H_2 molecule is used up to leave the grain, and the remainder is split between translation, rotation, and vibration of the new molecule. The exact level distribution of newly formed H_2 is yet unknown, but it could very well contribute to the observed excitation at intermediate energies, $E \approx 1-3$ eV (Black & van Dishoeck 1987; Le Bourlot et al. 1995).

Using Eq. 6 we can sum up the column densities of all levels with energy $E/k \geq 10\,000$ K, to find a column density 1.30×10^{18} cm^{-2}, a fraction 6.8×10^{-4} of the total warm H_2 column. Could H_2 formation in a steady state produce such a fraction of molecules in highly excited states? The pumping rate due to formation pumping is equal to the H_2 formation rate, $n({\rm H}) n_{\rm H} R_{\rm gr}$, where $R_{\rm gr} \approx 5 \times 10^{-17}$ cm^3 s^{-1} is the H_2 formation rate coefficient per hydrogen nucleus. We estimate the radiative decay rate by starting with the characteristic radiative lifetime of $\sim 10^6$ sec for a molecule in a vibrational level $v \approx 5$, and note that ~ 5 jumps may be required to reach the ground state, so that the effective A-coefficient $A_{\rm x} \approx 2 \times 10^{-7}\, s^{-1}$. The population balance for the excited states then writes

$$R_{\rm gr}\ n_{\rm H}\ n({\rm H}) \ = \ n_{\rm x}({\rm H_2})\ A_{\rm x}, \qquad (8)$$

which yields an excited H_2 fraction

$$\frac{n_{\rm x}({\rm H_2})}{n({\rm H_2})} \ = \ \frac{n({\rm H})}{n({\rm H_2})} \frac{n_{\rm H} R_{\rm gr}}{A_{\rm x}}$$
$$= \ 5 \times 10^{-4} \left(\frac{n_{\rm H}}{10^6 {\rm cm}^{-3}} \ \ \frac{n({\rm H})}{2 n({\rm H_2})} \right) , \qquad (9)$$

which would be consistent with the observed value, if the term in brackets assumes a value of order unity. This simple estimate thus shows that H_2 formation could account for some of the high excitation level populations if the density is high, the atomic fraction not small, and the formation rate coefficient in the warm shocked gas is somewhat higher than the value implied at ≈ 100 K from Copernicus observations, which is $R_{\rm gr} \approx 3 \times 10^{-17}$ cm^3 s^{-1} (Jura 1975).

To illustrate the possible importance of H_2 formation for the high-excitation level pumping we show that a simple superposition of two gas layers with hydrogen nuclei density $n_{\rm H} = 10^6 {\rm cm}^{-3}$, atomic fraction $n({\rm H})/n_{\rm H} = 0.5$, and respective temperatures of 200 K and 800 K, with column densities $N_{\rm H_2} = 1.2 \times 10^{22} {\rm cm}^{-2}$ and $1.2 \times 10^{21} {\rm cm}^{-2}$, can in fact reproduce the observed level column distribution better than any shock model currently available. We used the photodissociation front code of Draine & Bertoldi (1996), but without UV illumination, to compute the non-LTE level distributions for gas at a fixed temperature, density, and molecular fraction. We include H_2 formation with a rate coefficient $R_{\rm gr} \ = \ 5 \times 10^{-17} {\rm cm}^3 {\rm s}^{-1}$ and assume a level distribution for the newly formed H_2 following $N(v,J) \propto (2J+1) e^{-E(v,J)/kT_{form}}$, with a "formation temperature" $T_{form} = 5000$ K chosen to match the slope of the observed high-excitation level distribution.

Fig. 11 illustrates how the newly-formed H_2 molecules give rise to a high-excitation tail in the levels' column density distribution. The remaining gas displays a thermal distribution at least up to the levels which are mainly populated by H_2 formation.

Non-thermal collisions: An even more important pumping mechanism for the high-excitation levels may be non-

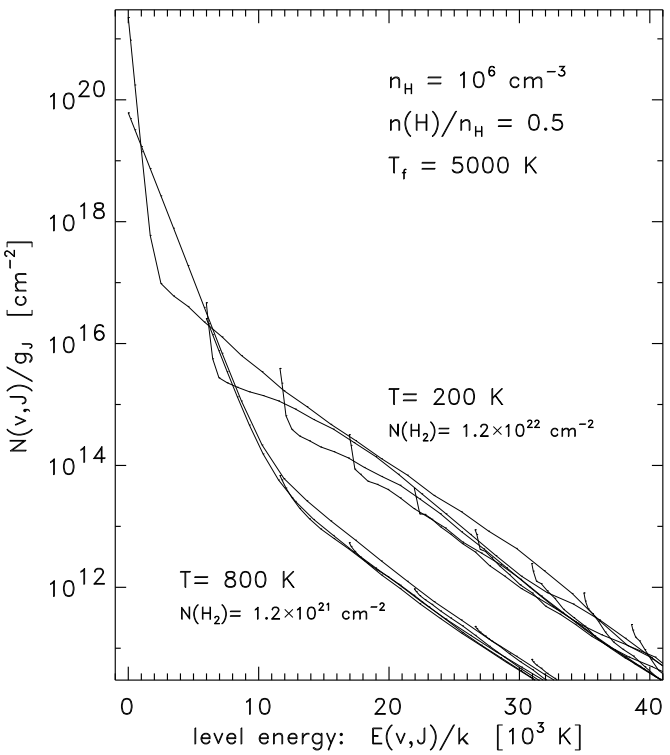

Fig. 11. Level column density distributions for two gas layers at temperatures 200 K and 800 K with H_2 column densities of 1.2×10^{22}cm^{-3} and 1.2×10^{21}cm^{-3}, respectively. Individual vibrational level distributions are shown as separate lines. The sum of both distributions well matches the observed level distribution toward Peak 1 which is shown in Fig. 7.

thermal collisions between molecules and ions in a magnetic shock. In magnetic C-type shocks, which are believed to be responsible for most of the emission in Peak 1, the gas is accelerated through fast inelastic collisions. In a magnetic precursor the ions, which are tied to the magnetic field, collide with the undisturbed pre-shock gas at relative velocities comparable to the shock speed. Such non-thermal ion–molecule collisions lead to the acceleration of the molecules and to their internal excitation. High-velocity molecules subsequently collide with other molecules, leading to a cascade of collisions during which the relative kinetic energy is in part converted to internal excitation of the molecules (O'Brien & Drury 1996). In sufficiently fast C-shocks, the ion–H_2 and H_2–H_2 collisions can even lead to a significant collisional dissociation rate. The molecules dissociated in a steady-state, partially dissociative shock reform further downstream, so that across such a shock the H_2 dissociation rate equals the H_2 reformation rate. For every collisionally dissociated molecule there will be a larger number of inelastic collisions which did not lead to dissociation, but to the excitation of the molecule into high ro-vibrational states, up to the dissociation limit. The high-excitation H_2 level column densities thereby created should therefore be larger than those caused by H_2 formation alone.

Note that such energetic collision between ions and H_2 in C-shocks are relatively infrequent because ions are rare – thus the excited H_2 has time enough to cascade to lower levels between collisions, giving rise to line emission from the highly excited levels. In C-type shocks, however, dissociations take place too quickly for highly excited H_2 to radiatively decay.

We conclude that non-thermal collisions in partially dissociative C-shocks could pump the high-excitation states in the H_2 electronic ground state to the levels observed. However, no detailed shock models are available yet which account for this process.

0 – 0 S(25): The $J = 27$ level observed through the $0-0$ S(25) line appears overpopulated by a factor of seven over what would be expected from the least-squares fit of the data shown in Fig. 8. The $J = 27$ level is 3.6 eV above ground and only 0.9 eV from the dissociation limit. H_2 molecules which are newly formed on grains are unlikely to be able to populate states so high, because some fraction of the formation energy is lost to overcome the grain surface potential, and some goes to kinetic and vibrational excitation. Unless we misidentified the $0-0$ S(25) line, it appears that a different mechanism may be populating this level and possibly other high levels. The gas-phase formation of H_2 via H^-, e.g., might be able to leave the new molecule in such a high rotational state (Bieniek & Dalgarno 1979; Black et al. 1981; Launay et al. 1991).

3.4.4. Comparison with shock models

For over 20 years, evidence accumulated that the H_2 emission from OMC-1 may arise from shocks (Gautier et al. 1976; Kwan & Scoville 1976). However, the physical nature of these shocks remains unclear. Models for planar J-type (Hollenbach & Shull 1977; Kwan 1977; London et al. 1977) or C-type (Draine 1980; Draine & Roberge 1982; Chernoff et al. 1982; Draine et al. 1983) shocks were unable to reproduce the observed wide velocity profiles (Nadeau & Geballe 1979; Brand et al. 1989b; Moorhouse et al. 1990; Chrysostomou et al. 1997), or the wide range of excitation conditions observed. Bow shocks were suggested to account for the observed range of excitation conditions and the wide velocity profiles (Hartigan et al. 1987; e. g. Smith et al. 1991a, 1991b), but it remains unclear whether these are predominantly C-type, J-type, or a combination of those.

Planar shock models: In Sect. 3.3 we suggested that some fraction of the fine structure line emission may arise from dissociative J-shocks with velocities of about 85 km s^{-1}, pre-shock densities $n_{\rm H} \approx 10^5 - 10^6\,{\rm cm}^{-3}$, and a beam

filling factor of 3–4 (Hollenbach & McKee 1989). In such dissociative shocks most of the excitation of the $v = 0$, $J \leq 5$ levels is collisional, and the emission arises in the H_2 reformation region where the temperature levels at 400 to 500 K, which is somewhat below the observed excitation temperature of the lowest levels. The higher levels would then be predominantly pumped by newly formed molecules. Such a model however neither fits the low excitation nor the higher excitation level populations very well. The deficits of the J-shock model could be compensated if we combined it with a C-shock model, e.g., one of Kaufman & Neufeld (1996) with $v_s = 25$ km s^{-1}, $n_{H_2} = 10^5 - 10^6$ cm^{-3}, and a beam filling factor 0.3. Such a combined model provides a good fit to the $v = 0$, $J = 3$ to 9 level populations, although higher rotational level populations are predicted too large (see Fig. 12: HK).

A combination of J-type and C-type shocks would be consistent with the picture proposed by Chernoff et al. (1982), who suggested that a high velocity, $\sim$ 110 km s^{-1}, wind emanating from an object near IRc2 drives a $\sim$ 30 km s^{-1} expanding shell of swept-up material. The low beam filling factor of the C-shock emission could be due to the clumping of the ambient medium.

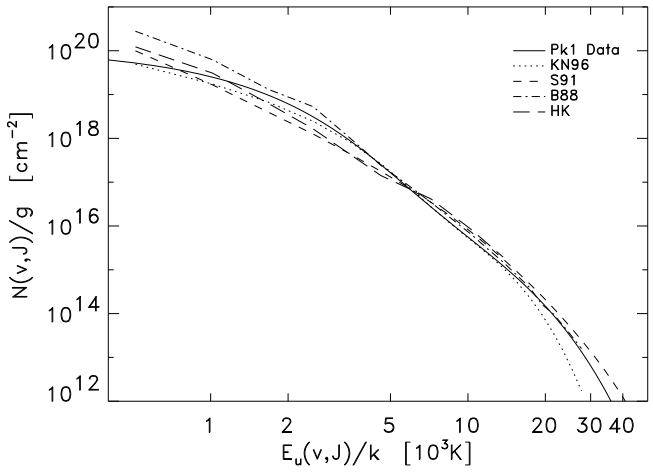

Fig. 12. Comparison of the observed H_2 level column distribution (solid line) with models: dissociative J-shock plus C-shock model (HK: long-dashed), J-type cooling flow model (B88: dash-dotted), bow shock model (S91: short-dashed), combination of two planar C-shock models (KN96: dotted).

The H_2 level populations implied by previous ground-based observations (e.g. Brand et al. 1988; Parmar et al. 1994; Burton & Haas 1997) were attempted to match with an empirical planar J-shock "cooling flow" model (Brand et al. 1988; Chang & Martin 1991; Burton & Haas 1997), which assumes that the cooling is dominated by H_2, and cooling by other molecules such as H_2O and CO may be neglected. Such a model can match the medium and high-excitation level populations, although it somewhat overestimates the population of lower rotational levels. These models assume LTE level distributions, which as we argued above, may not be a valid assumption for the high-excitation levels if the gas density is below 10^6cm^{-3}. Furthermore, theoretical chemical studies show that most oxygen not locked in CO is converted to H_2O (Draine et al. 1983; Kaufman & Neufeld 1996), which is detected by ISO-LWS observations toward OMC-1 (Harwit et al. 1998; Cernicharo et al. 1999). Both H_2O and CO should therefore be significant coolants, and the neglect of this in these models is worrisome.

Currently available more realistic single shock models do not seem to fit the observed H_2 level distribution. It appears necessary to combine at least two shock models, one to account for the high-excitation level populations, one for the low-excitation levels. For example, combining two models from Kaufman & Neufeld (1996), with shock velocities of 20 and 40 km s^{-1}, and beam filling factors of 1 and 0.026, respectively, can well match the level population up to $E/k \approx 20\,000$ K (Fig. 8, KN96); a pre-shock H_2 number density of 3×10^5 cm^{-3} was adopted. The Kaufman & Neufeld models however do not account for time-dependency, formation pumping, or non-thermal excitation.

H_2 velocity dispersion: Optical and near-IR observations with high spectral resolution toward the OMC-1 outflow show that typical FWHM widths of the H_2 lines are 50–60 km s^{-1} (Nadeau & Geballe 1979; Moorhouse et al. 1990; Geballe & Garden 1987; Chrysostomou et al. 1997), and that the line wings can extend to several hundred km s^{-1} (Ramsey-Howat et al., in prep.). Molecular hydrogen is expected to be destroyed in shocks with velocities larger than 30 to 50 km s^{-1}, depending on the magnetic field strength. It is therefore puzzeling how the H_2 emission can show such large velocity dispersions, even in filaments which are only several arcseconds in size.

Bow-shocks: It has been suggested that the H_2 emission arises in bow-shocks, in which the effective shock velocity decreases from the tip to the wake. The shock speed at the apex may be high enough to produce a dissociative J-shock here. But further down the wake, non-dissociative C-type shocks can prevail, with peak temperatures in the shocked molecular layers that decrease steadily down the wake. Thereby a large range of temperatures for the molecular gas exists in a single bow shock. This could account for the observed level excitation, and may also explain the observed constancy of H_2 excitation over the entire OMC-1 outflow (Brand et al. 1989a).

The existence of bow-shocks is also supported by the observation of double-peaked velocity profiles for isolated regions in the outflow (Chrysostomou et al. 1997), and

of knots of [Fe II] emission which coincide with "fingers" of H_2 emission. Allen & Burton (1993) suggest that the [Fe II] and H_2 emission trace tips and wakes of bow shocks formed in a stellar outflow.

Recent observations of [Fe II] and H_2 1-0 S(1) velocity profiles (Tedds et al. 1999) however question the bow shock picture. Alternatively, Stone et al. (1995) proposed that the bows result from Rayleigh-Taylor instabilities when a poorly collimated outflow accelerates in an ambient medium of decreasing density, or when catching up with a slower shock.

It is difficult to understand how the high velocity excited H_2 can be produced in a bow shock which is produced, e.g., by a dense bullet which is moving through a medium initially at rest. Ambient gas which has passed through parts of the bow shock which are not strong enough to dissociate the H_2 will not be accelerated to velocities much larger than 30 km s^{-1}, unless the magnetic field is very strong. If alternatively the bow shock arises from a molecular wind impinging on a dense obstacle, then the problem arises how the molecular wind was accelerated to over 100 km s^{-1} without destroying the molecules, and why we do not see a lot more mass, traced by CO, e.g., at such high velocities.

Smith et al. (1991a) are able to reproduce the shape and width of the observed H_2 lines in the Orion outflow with bow shock models, but only by assuming a magnetic field strength of 50 mG, significantly higher than the 10 mG implied by polarization studies (Chrysostomou et al. 1994).

In Fig. 12, we compare our data with a bow shock model by Smith (1991b), adopting a peak shock velocity of 100 km s^{-1} and an Alfvén speed of 2 km s^{-1}. This model is able to match the medium-excitation level populations well, but underestimates the low-excitation, and overestimates the high-excitation levels.

Note that the H_2 excitation in the models of Smith, like for the planar J-shock model of Brand et al. (1988), was calculated under the assumption of LTE, and also it ignores non-thermal excitation mechanisms. These models therefore overestimate the population of the high energy levels by thermal collision, and at the same time they underestimate the level population because they neglect non-thermal excitation mechanisms.

We conclude that current shock models are able to reproduce the overall H_2 level distribution only when combining shocks with a range of velocities. However, most models do not include the physics most likely to account for the highest excitation level populations.

4. Summary

We obtained spectra with the ISO short wavelength spectrometer of the 2.4–45 μm emission toward the brightest H_2 emission peak of the Orion OMC-1 outflow. In those spectra we detected a large number of H_2, H I, and atomic/ionic fine structure lines.

1. Estimating the extinction from relative line intensities we find that the atomic hydrogen emission originates in the foreground H II region, whereas the H_2 emission comes from the shock-excited gas within the star-forming molecular cloud.
2. Most of the atomic fine structure emission originates in the foreground H II region and its bordering photodissociation front.
3. The [S I]25μm line and some fraction of the [Si II]34.8μm and [Ne II]12.8μm emission could arise in strong J-shocks.
4. The total warm ($T >$ a few hundred K) H_2 column density is $(1.9 \pm 0.5) \times 10^{21}$ cm^{-2}, and the total warm H_2 mass in the ISO-SWS aperture is (0.06 ± 0.015) $M_\odot$. The total H_2 luminosity within the ISO-SWS aperture is (17 ± 5) $L_\odot$, and when extrapolated to the entire outflow, (120 ± 60) $L_\odot$.
5. The H_2 excitation reveals no signs of fluorescence or a deviation from an ortho-to-para ratio of three.
6. The H_2 level column density distribution shows an excitation temperature which increases from about 600 K for the lowest rotational and vibrational levels to about 3200 K at level energies $E(v, J)/k > 14\,000$ K.
7. No single steady-state shock model can reproduce the observed H_2 level populations. To match both the low- and high-excitation level populations, a combination of slow and fast shocks is required, or time-dependent magnetic shocks which include transient J-shocks. Most shock models lack the processes that are likely to populate the high energy H_2 levels.
8. The higher energy H_2 levels may be excited either thermally in non-dissociative J-shocks, through non-thermal collisions between fast ions and molecules with H_2 in C-shocks, or they are due to newly formed H_2 molecules.
9. In a most simple model, the overall level distribution of the observed H_2 is well reproduced by two columns of warm, partially dissociated gas at H nuclei density $10^6 cm^{-3}$, with respective temperatures of 200 K and 800 K and a column density ratio of 10 to 1. In this model the high-excitation tail in the H_2 level populations is due to H_2 formation.
10. The highest-excitation line we detected, 0–0 S(25), implies a column density of the $v = 0,\ J = 27$ level way above what we would expect from the extrapolated excitation of the lower energy levels. A different pumping mechanism, such as the gas phase formation of H_2 via H^-, might be responsible for the population of the highest energy levels.

ACKNOWLEDGMENTS

We are very thankful to C. Wright, A. Poglitsch, D. Lutz, L. Looney, M. Lehnert, and M. Walmsley for valuable

comments, to A. Schultz for providing the NICMOS image, to B. Rubin for providing unpublished results from his H II region model, to B.T. Draine for his contributions to the non-LTE H_2 models and his careful reading of the manuscript, to M. Smith for providing the H_2 line strengths for his bow shock model, and to the SWS Data Center at MPE, especially to H. Feuchtgruber and E. Wieprecht.

References

Allen, D. A. & Burton, M. G. 1993, Nature, 363, 54
Bachiller, R. & Perez Gutierrez, M. 1997, ApJ, 487, L93
Beckwith, S., Persson, S., Neugebauer, G., & Becklin, E. 1978, ApJ, 223, 464
Bertoldi, F. 1997, in Proceedings of the first ISO workshop on Analytical Spectroscopy, Eds. A. M. Heras, et al. Noordwijk: ESA Publications Division (ESA SP-419), 67
Bertoldi, F., Timmermann, R., Rosenthal, D., Drapatz, S., & Wright, C. .M. 1999, A&A, 346, 267
Bertoldi, F., Draine, B.T., R., Rosenthal, D., Timmermann, R., Ramsay Howat, S.K., Geballe, T., Feuchtgruber, H., Drapatz, S. 2000 in *Astrochemistry: From Molecular Clouds to Planetary Systems*, Proc. of the IAU Symp. 197, Y. C. Minh & E. F. van Dishoeck (eds), 565
Bieniek, R. J., Dalgarno, A. 1979, ApJ, 228, 635
Black, J. H., Porter, A., & Dalgarno, A. 1981, ApJ, 249, 138
Black, J. H. & van Dishoeck, E. F. 1987, ApJ, 322, 412
Boonman, A., Rosenthal, D., Wright, C., van Dishoeck, E. F, & Drapatz, S. in preparation
Brand, P., Moorhouse, A., Burton, M., Geballe, T., Bird, M., & Wade, R. 1988, ApJ, 334, L103
Brand, P., Toner, M., Geballe, T., Webster, A., Williams, P., & Burton, M. 1989a, MNRAS, 237, 929
Brand, P. W. J. L., Toner, M. P., Geballe, T. R., & Webster, A. S. 1989b, MNRAS, 237, 929
Burton, M. G., Hollenbach, D. J., & Tielens, A. G. G. M. 1990a, 365, 620
Burton, M. G. & Puxley, P. 1990b, in The Interstellar Medium in External Galaxies: Summaries of Contributed Papers, ed. D. Hollenbach & H. Thronson, NASA CP, 3084,238
Burton, M. G., Hollenbach, D. J., & Tielens, A. G. G. M. 1992, 399, 563
Burton, M. & Haas, M. 1997, A&A, 327, 309
Caselli, P., Hartquist, T. W., & Havnes, O. 1997, A&A, 322, 296
Cernicharo, J., González-Alfonso, E., Sempere, M. J., Leeks, S., van Dishoeck, E., Wright, C., Lim, T., Cox, P., & Pérez-Martínez, S. 1999, in *The Universe as seen by ISO*, ESA proc., P. Cox & M. Kessler (eds), 565
Chang, C. A. & Martin, P. G. 1991, ApJ, 378,202
Chernoff, D., Hollenbach, D., & McKee, C. 1982, ApJ, 259, L97
Chièze, J.-P., Pineau des Forêts, & G., Flower, D. 1998, MNRAS, 295, 672
Chrysostomou, A., Hough, J., Burton, M. G., & Tamura, M. 1994, MNRAS, 268, 325
Chrysostomou, A., Burton, M. G., Axon, D. J., Brand, P. W. J. L., Hough, J. H., Bland-Hawthorn, J., & Geballe, T. R. 1997, MNRAS, 289, 605
Davis, C. J. & Smith, M. D. 1996, A&A, 310, 961
de Graauw,Th., Haser, L., Beintema, D. et al. 1996, A&A, 315, L49
Dougados, C., Léna, P., Ridgway, S., Christou, J., & Probst, R. 1993 ApJ, 406, 112
Draine, B. T. 1980, ApJ, 241, 1081
Draine, B. T. & Roberge, W. G. 1982, ApJ, 259, L91
Draine, B. T., Roberge, W., & Dalgarno, A. 1983, ApJ, 264, 485
Draine, B. T. & Lee, H. 1984, 285, 89
Draine, B. T. 1989, in: Proc. of 22nd ESLAB Symposium Infrared Spectroscopy in Astronomy, p. 93
Draine, B. T. & Bertoldi, F. 1996, ApJ, 468, 269
Draine, B. T. & Bertoldi, F. 2000, in H_2 in Space, ed. Combes & Pineau des Forêts
Everett, M. E., DePoy, D. L., & Pogge, R. W. 1995, AJ, 110, 1295
Flower, D., Pineau des Forêts, G. 1999, MNRAS 308, 271
Fuente, A., Martin-Pintado, J. Rodriguez-Fernandez, N. J., de Vincente, P., & Kunze, D. 1999, ApJ, 518, L45
Garden, R. 1986, PhD Diss., Univ. Edinburgh
Gautier, T.,Fink, U.,Treffers, R., & Larson, H. 1976, ApJ, 207, L129
Geballe, T. R. & Garden, R. 1987, ApJ, 317, L107
Genzel, R. & Stutzki, J. 1989, ARA&A, 27,41
Goetz, J. A., Pipher, J. L., Forrest, W. J., Watson, D. M., Raines, S. N., Woodward, C. E., Greenhouse, M. A., Smith, H. A., Hughes, V. A., & Fischer, J. 1998 ApJ, 504, 359
Haas, M. R., Hollenbach, D., & Erickson, E. F. 1991, ApJ, 374, 555
Hartigan, P., Raymond, J., & Hartmann, L. 1987, ApJ, 316, 323
Harwit, M., Neufeld, D. A., Melnick, G. J., & Kaufman, M. J. 1998, ApJ, 497, L105
Herrmann, F., Madden, S. C., Nikola, T., Poglitsch, A., Timmermann, R., Geis, N., Townes, C. H., & Stacey, G. 1997, ApJ, 481, 343
Hollenbach, D. & Shull, M. 1977, ApJ, 216, 419
Hollenbach, D. & McKee, C. F. 1989, ApJ, 342, 306
Jura, M. 1975, ApJ, 197, 575
Kaufman, M. J. & Neufeld, D. 1996, ApJ, 456, 611
Kessler, M., Steinz, J., Anderegg, M. et al. 1996, A&A, 315, L27
Kwan, J. & Scoville, N. 1976, ApJ, 210, L39
Kwan, J. 1977, ApJ, 216, 713
Launay, J. M., Le Dourneuf, M., & Zeippen, C. J. 1991, A&A, 252, 842
Le Bourlot, J., Pineau des Fôrets, G., Roueff, E., Dalgarno, A., & Gredel, R. 1995, 449, 178
Le Bourlot, J., Pineau des Fôrets, G., & Flower, D. R. 1999, MNRAS, 305, 802
London, R., McCray, R., & Chu,S-I. 1977, ApJ, 217, 442
Martin-Pintado, J., Bachiller, R., & Fuente, A. 1992, A&A, 254, 315
Menten, K. M. & Reid, M. J. 1995, ApJ, 445, L157
Moorhouse, A., Brand, P., Geballe, T., & Burton, M. 1990, MNRAS, 242, 88
Nadeau, D. & Geballe, T. 1979, ApJ, 230, L169
O'Brien, I., Drury, L. 1996, MNRAS, 280, 550
Parmar, P. S., Lacy, J. H., & Achtermann, J. M. 1994, ApJ, 430, 786

Pegourie, B. & Papoular, R. 1985, 142, 451
Rubin, R. H., Simpson, J. P., Haas, M. R., & Erickson, E. F. 1991, ApJ, 374, 564
Schultz, A. S. B., Colgan, S. W. J., Erickson, E. F., Kaufman, M. J., Hollenbach, D. J., O'Dell, C. R., Young, E. T., &. Chen, H. 1999, ApJ, 511, 282
Smith,M., Brand, P., & Moorhouse, A. 1991a, MNRAS, 248, 730
Smith,M. 1991b, MNRAS, 253, 175
Stacey, G. J., Gull, G. E., Hayward, T. L., Latvakoski, H., & Peng, L. 1995, in *Airborne Astronomy Symposium on the Galactic Ecosystem*, ASP conf. ser., Vol. 73, M. R. Haas, J. A. Davidson & E. F. Erickson, p. 215
Sternberg, A. & Neufeld, D. A. 1999 ApJ, 516, 371
Stone, J. M., Xu, J., & Mundy, L. G. 1995, Nature, 377, 315
Storey, P. & Hummer, D. 1995, MNRAS, 272, 41
Tedds, J., Brand, P., & Burton, M. 1999, MNRAS, 307, 337
Tielens, A. G. G. M. & Hollenbach, D. 1985a, ApJ, 291, 722
Tielens, A. G. G. M. & Hollenbach, D. 1985b, ApJ, 291, 747
Timmermann, R., Bertoldi, F., Wright, C., Drapatz, S., Draine, B., Haser, L., & Sternberg, A. 1996a, A&A, 315, L281
Timmermann, R. 1996b, ApJ, 456, 631
Turner, J., Kirby-Docken, K., & Dalgarno A. 1977, ApJS, 35, 281
van Dishoeck, E. F., Helmich, F. P., Schutte, W. A., et al. 1998, in *Star Formation with ISO*, ASP vol. 132, p. 54, J. Yun & R. Liseau (eds)
Verstraete, L., Puget, J. L., Falgarone, E., Drapatz, S., Wright, C., & Timmermann, R. 1996, 315, L337
Volk, K. & Kwok, S. 1988, ApJ, 331, 435
Walmsley, C. M., Pineau des Forêts, G., & Flower, D. R. 1999, A&A, 342, 542
Wolniewicz, L., Simbotim, I., & Dalgarno, A. 1998, ApJS, 115, 293

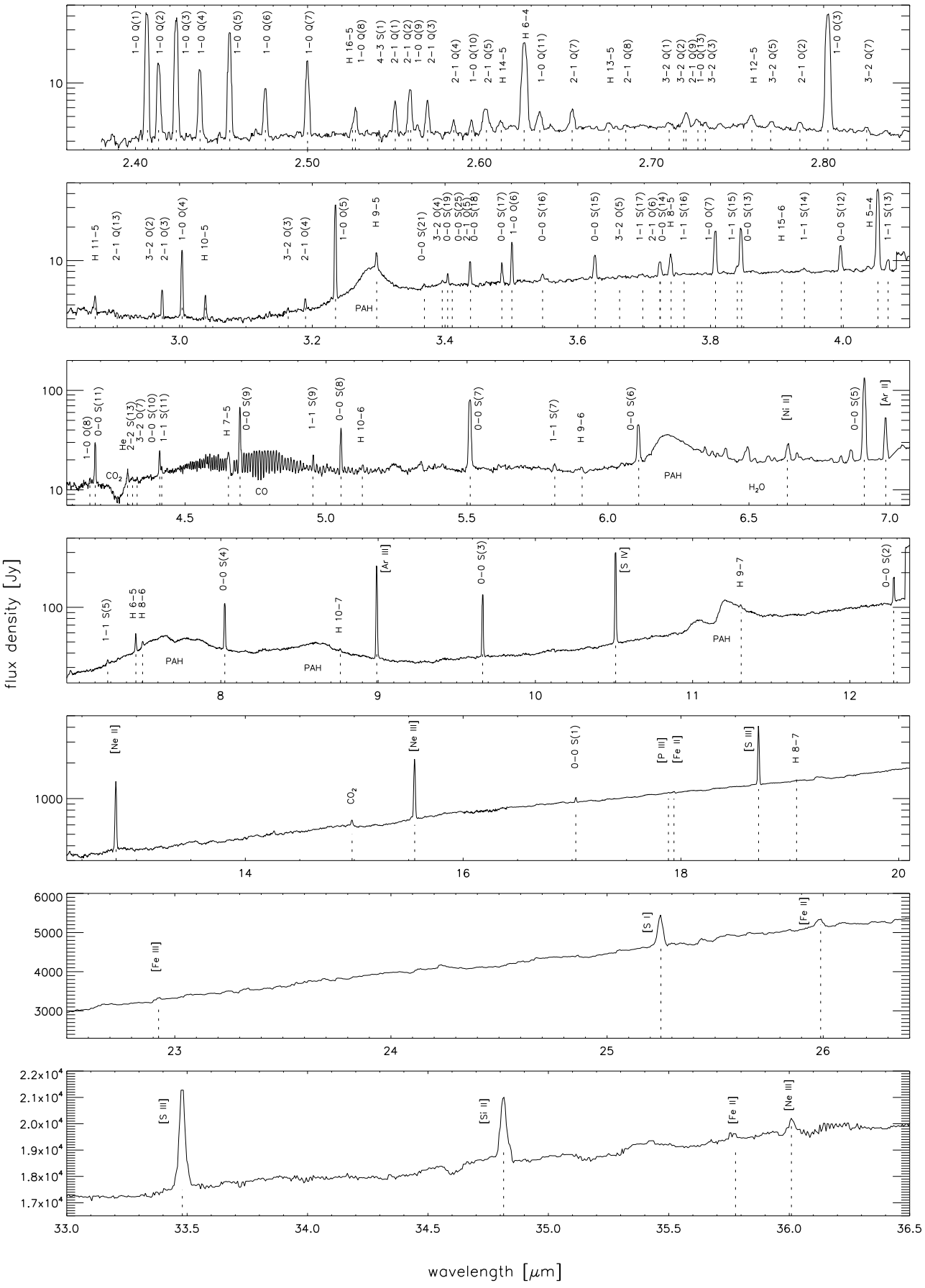

Fig. 3. The full scan SWS 01 spectrum of Fig. 2 in detail.

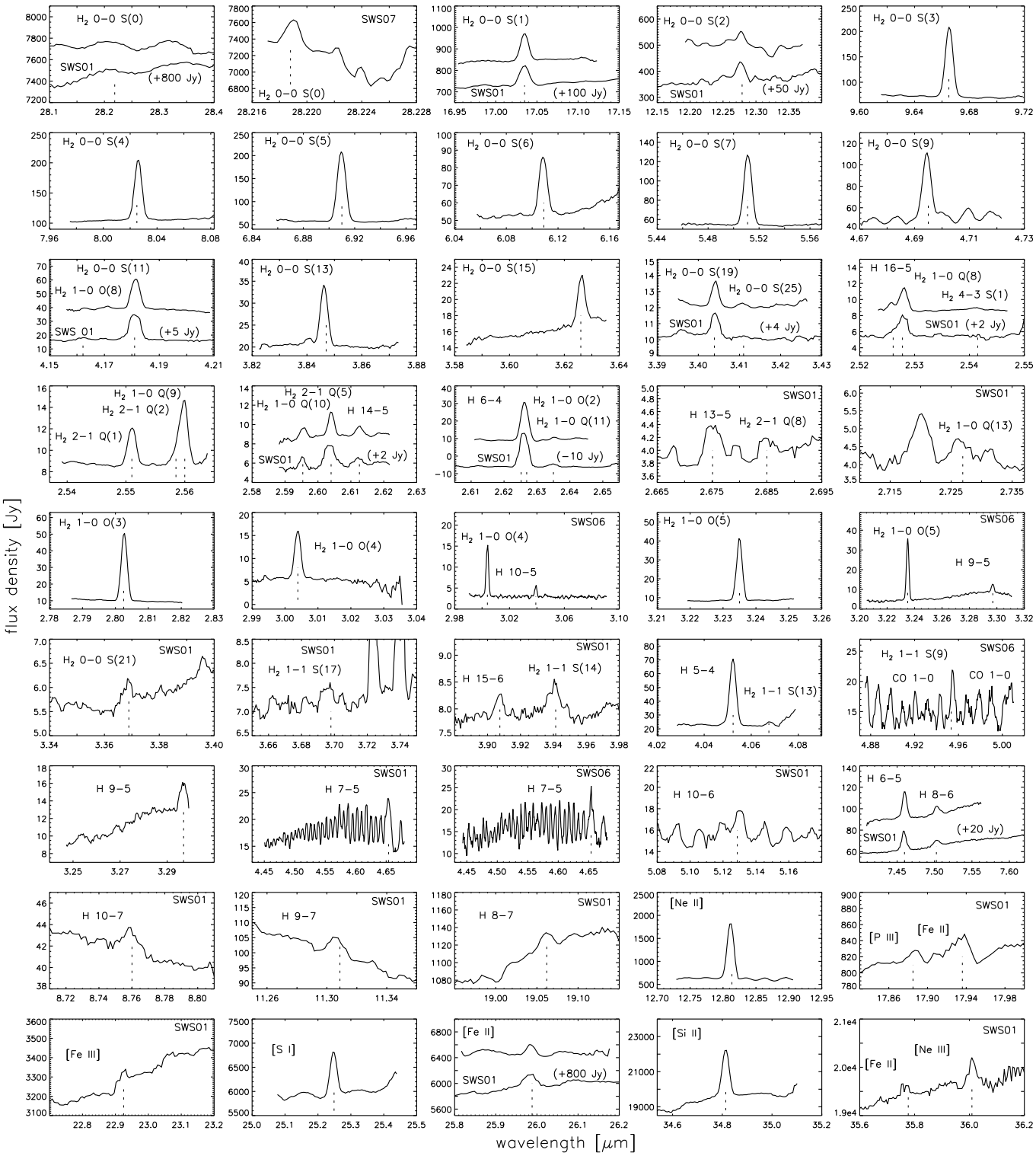

Fig. 4. Line scans in the SWS 02 or SWS 07/SWS 06 modes. In cases where the flux from the SWS 01 full scan spectrum differs much from that found in other observing modes, or where lines do not show well in Figs. 2 and 3, we overplot the SWS 01 spectrum for comparison.

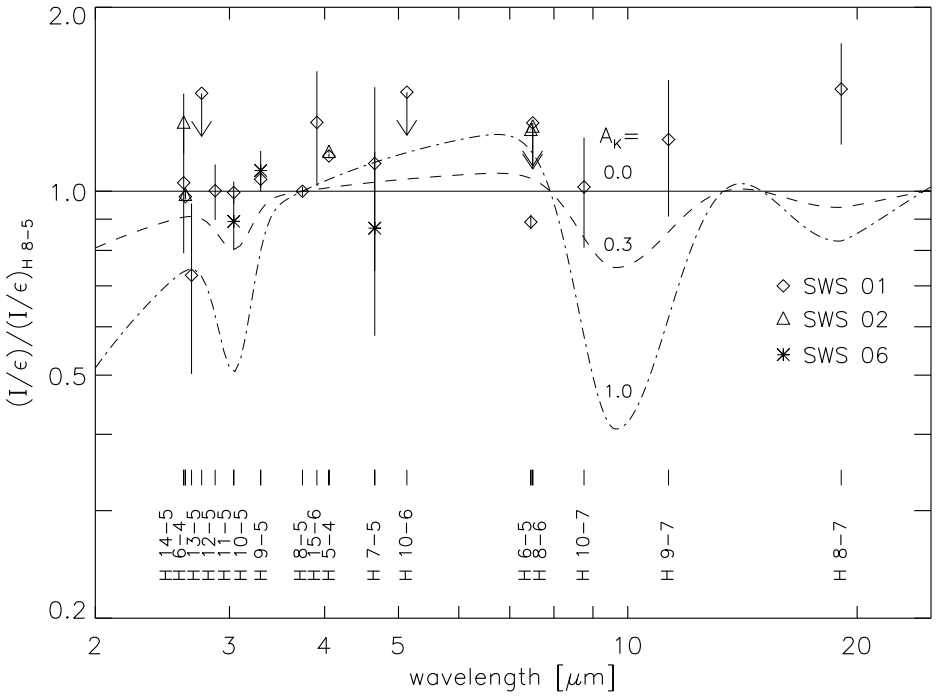

Fig. 7. An attempt to derive the differential extinction in the H recombination line emission: The line intensities divided by their respective emissivities are normalized by this value for the H 8–5 line, and then plotted against line wavelength. With no differential extinction to the H 8–5 line, all data points should line up at unity value. The broken lines show the expected distribution of values adopting the shape of the extinction curve derived from H_2 lines (Fig.6), with two different values of the absolute extinction at K. The apparent distribution is consistent with an extinction of zero.

Table 3. Summary of the ISO-SWS H_2 line observations at Orion Peak 1

line	λ [μm]	E_u/k [a] [K]	A [b] [s^{-1}]	SWS AOT	I_{obs} [c] [erg $s^{-1}cm^{-2}sr^{-1}$]	S/N[d]	A_λ [e] [mag]	N_u [f] [cm^{-2}]
0-0 S(0)	28.2188	509.9	2.94×10^{-11}	01	$< 7.90 \times 10^{-4}$	$< 3.$	0.27	$< 6.17 \times 10^{21}$
0-0 S(1)	17.0346	1015.0	4.76×10^{-10}	01	1.34×10^{-3}	27.8	0.53	4.92×10^{20}
				02	1.71×10^{-3}	51.4	0.53	6.28×10^{20}
0-0 S(2)	12.2785	1682.0	2.76×10^{-9}	01	1.44×10^{-3}	32.8	0.57	6.84×10^{19}
				02	1.78×10^{-3}	12.6	0.57	8.46×10^{19}
0-0 S(3)	9.6649	2503.4	9.84×10^{-9}	01	4.08×10^{-3}	200.0	1.35	8.82×10^{19}
				02	4.72×10^{-3}	251.0	1.35	1.02×10^{20}
0-0 S(4)	8.0258	3474.6	2.64×10^{-8}	01	4.43×10^{-3}	133.0	0.45	1.28×10^{19}
				02	4.84×10^{-3}	231.0	0.45	1.40×10^{19}
1-1 S(5)	7.2807	10 340.3	5.44×10^{-8}	01	2.48×10^{-4}	6.7	0.18	2.48×10^{17}
0-0 S(5)	6.9091	4586.7	5.88×10^{-8}	01	1.09×10^{-2}	63.7	0.15	9.31×10^{18}
				02	1.15×10^{-2}	64.2	0.15	9.83×10^{18}
0-0 S(6)	6.1089	5829.8	1.14×10^{-7}	01	3.37×10^{-3}	44.2	0.17	1.33×10^{18}
				02	3.03×10^{-3}	58.3	0.17	1.20×10^{18}
1-1 S(7)	5.8111	12 816.4	1.82×10^{-7}	01	2.48×10^{-4}	8.1	0.18	5.91×10^{16}
0-0 S(7)	5.5115	7196.6	2.00×10^{-7}	01	9.99×10^{-3}	113.0	0.20	2.09×10^{18}
				02	8.33×10^{-3}	141.0	0.20	1.74×10^{18}
0-0 S(8)	5.0528	8677.1	3.24×10^{-7}	01	2.28×10^{-3}	24.8	0.23	2.78×10^{17}
1-1 S(9)[g]	4.9533	15 725.5	4.38×10^{-7}	01	4.65×10^{-4}	4.5	0.24	4.14×10^{16}
				06	2.81×10^{-4}	4.1	0.24	2.50×10^{16}
0-0 S(9)[g]	4.6947	10 261.2	4.90×10^{-7}	01	5.09×10^{-3}	15.7	0.26	3.92×10^{17}
				02	4.85×10^{-3}	26.9	0.26	3.73×10^{17}
1-1 S(11)	4.4171	18 977.1	8.42×10^{-7}	01	2.13×10^{-4}	4.6	0.29	9.21×10^{15}
0-0 S(10)	4.4096	11 940.2	7.03×10^{-7}	01	1.26×10^{-3}	18.2	0.29	6.52×10^{16}
3-2 O(7)	4.3298	19 092.2	9.77×10^{-8}	01	$< 6.54 \times 10^{-5}$	< 3	0.30	$< 2.41 \times 10^{16}$
2-2 S(13)	4.3137	27 264.3	1.14×10^{-6}	01	$< 7.47 \times 10^{-5}$	< 3	0.30	$< 2.35 \times 10^{15}$
0-0 S(11)	4.1810	13 702.7	9.64×10^{-7}	01	2.39×10^{-3}	31.7	0.32	8.77×10^{16}
				02	2.19×10^{-3}	113.0	0.32	8.03×10^{16}
1-0 O(8)	4.1622	9285.7	7.38×10^{-8}	01	1.91×10^{-4}	3.7	0.32	9.13×10^{16}
				02	1.10×10^{-4}	7.9	0.32	5.26×10^{16}
1-1 S(13)	4.0675	22 516.4	1.38×10^{-6}	01	2.39×10^{-4}	13.7	0.33	6.17×10^{15}
				02	1.80×10^{-4}	8.7	0.33	4.55×10^{15}
0-0 S(12)	3.9968	15 538.5	1.27×10^{-6}	01	6.50×10^{-4}	41.5	0.34	1.78×10^{16}
1-1 S(14)	3.9414	24 372.4	1.69×10^{-6}	01	1.03×10^{-4}	6.5	0.35	2.09×10^{15}
0-0 S(13)	3.8464	17 437.7	1.62×10^{-6}	01	1.51×10^{-3}	78.2	0.36	3.17×10^{16}
				02	1.40×10^{-3}	92.7	0.36	2.94×10^{16}
1-1 S(15)	3.8404	26 257.2	2.00×10^{-6}	01	1.09×10^{-4}	7.2	0.36	1.85×10^{15}
				02	1.51×10^{-4}	10.8	0.36	2.57×10^{15}
1-0 O(7)	3.8075	8364.9	1.06×10^{-7}	01	1.43×10^{-3}	99.3	0.37	4.57×10^{17}
1-1 S(16)	3.7602	28 199.5	2.32×10^{-6}	01	$< 1.51 \times 10^{-5}$	< 3	0.38	$< 2.19 \times 10^{14}$
2-1 O(6)	3.7236	13 150.2	2.28×10^{-7}	01	$< 3.72 \times 10^{-4}$	< 15.3	0.38	$< 5.47 \times 10^{16}$
0-0 S(14)	3.7245	19 408.7	2.41×10^{-6}	01	$< 3.72 \times 10^{-4}$	< 15.3	0.38	$< 5.18 \times 10^{15}$
1-1 S(17)	3.6979	30 156.2	2.64×10^{-6}	01	6.21×10^{-5}	3.8	0.39	7.87×10^{14}
3-2 O(5)	3.6630	17 811.7	3.52×10^{-7}	01	$< 3.73 \times 10^{-5}$	< 3	0.39	$< 3.53 \times 10^{15}$
0-0 S(15)	3.6263	21 408.6	2.41×10^{-6}	01	6.15×10^{-4}	29.9	0.40	8.48×10^{15}
				02	6.49×10^{-4}	31.2	0.40	8.94×10^{15}
0-0 S(16)	3.5470	23 451.6	2.83×10^{-6}	01	2.81×10^{-4}	7.2	0.42	3.28×10^{15}
1-0 O(6)	3.5007	7583.7	1.50×10^{-7}	01	8.37×10^{-4}	54.5	0.43	1.84×10^{17}
0-0 S(17)	3.4856	25 537.8	3.26×10^{-6}	01	3.35×10^{-4}	23.1	0.44	3.39×10^{15}
2-1 O(5)	3.4384	12 550.2	3.18×10^{-7}	01	$< 4.31 \times 10^{-4}$	< 22.8	0.46	$< 4.51 \times 10^{16}$
0-0 S(18)	3.4384	27 638.4	3.68×10^{-6}	01	$< 4.31 \times 10^{-4}$	< 22.8	0.46	$< 3.89 \times 10^{15}$
0-0 S(19)	3.4039	29 767.7	4.08×10^{-6}	01	1.62×10^{-4}	15.1	0.48	1.34×10^{15}
				02	1.13×10^{-4}	17.2	0.48	9.31×10^{14}

Table 3. -Continued

line	λ [μm]	E_u/k [a] [K]	A [b] [s^{-1}]	SWS AOT	I_{obs} [c] [erg $s^{-1}cm^{-2}sr^{-1}$]	S/N [d]	A_λ [e] [mag]	N_u [f] [cm^{-2}]
3-2 O(4)	3.3958	17 380.1	4.87×10^{-7}	01	4.88×10^{-4}	6.5	0.49	3.38×10^{15}
0-0 S(20)	3.3809	31 898.5	4.45×10^{-6}	01	$< 1.43 \times 10^{-5}$	< 3	0.50	$< 1.09 \times 10^{14}$
0-0 S(21)	3.3689	34 040.8	4.78×10^{-6}	01	2.47×10^{-5}	4.0	0.52	1.77×10^{14}
0-0 S(22)	3.3663	36 149.7	5.06×10^{-6}	01	$< 1.91 \times 10^{-5}$	< 3	0.52	$< 1.30 \times 10^{14}$
0-0 S(23)	3.3718	38 299.5	5.27×10^{-6}	01	$< 1.91 \times 10^{-5}$	< 3	0.51	$< 1.24 \times 10^{14}$
0-0 S(24)	3.3876	40 419.6	5.42×10^{-6}	01	$< 1.42 \times 10^{-5}$	< 3	0.50	$< 8.88 \times 10^{13}$
0-0 S(25)	3.4108	42 515.1	5.50×10^{-6}	01	$< 3.33 \times 10^{-5}$	< 3	0.48	$< 2.03 \times 10^{14}$
				02	2.42×10^{-5}	4.1	0.48	1.48×10^{14}
0-0 S(26)	3.4417	44 573.2	5.51×10^{-6}	01	$< 3.27 \times 10^{-5}$	< 3	0.46	$< 1.97 \times 10^{14}$
0-0 S(27)	3.4855	46 650.3	5.43×10^{-6}	01	$< 3.27 \times 10^{-5}$	< 3	0.44	$< 1.82 \times 10^{14}$
0-0 S(28)	3.5375	48 640.3	5.28×10^{-6}	01	$< 3.86 \times 10^{-5}$	< 3	0.42	$< 2.41 \times 10^{14}$
0-0 S(29)	3.5996	50 619.9	5.04×10^{-6}	01	$< 4.56 \times 10^{-5}$	< 3	0.41	$< 3.00 \times 10^{14}$
1-0 O(5)	3.2350	6950.6	2.09×10^{-7}	01	3.24×10^{-3}	221.0	0.76	6.39×10^{17}
				02	3.05×10^{-3}	218.0	0.76	6.02×10^{17}
				06	3.05×10^{-3}	144.0	0.76	6.02×10^{17}
2-1 O(4)	3.1899	12 094.1	4.41×10^{-7}	01	1.25×10^{-4}	12.4	0.88	1.28×10^{16}
3-2 O(3)	3.1637	17 092.3	7.04×10^{-7}	01	4.08×10^{-5}	3.8	0.94	2.76×10^{15}
1-0 O(4)	3.0039	6471.5	2.90×10^{-7}	01	1.28×10^{-3}	119.0	1.11	2.32×10^{17}
				02	1.20×10^{-3}	70.5	1.11	2.18×10^{17}
				06	1.34×10^{-3}	49.6	1.11	2.43×10^{17}
2-1 O(3)	2.9741	11 789.1	6.40×10^{-7}	01	3.43×10^{-4}	24.4	1.07	2.71×10^{16}
3-2 O(2)	2.9620	16 948.5	1.41×10^{-6}	01	$< 1.98 \times 10^{-5}$	< 3	1.06	$< 6.96 \times 10^{14}$
2-1 Q(13)	2.9061	23 926.4	2.22×10^{-7}	01	$< 4.37 \times 10^{-5}$	< 3	0.95	$< 8.70 \times 10^{15}$
3-2 Q(7)	2.8250	20 861.9	3.58×10^{-7}	01	$< 4.84 \times 10^{-5}$	< 3	0.80	$< 5.07 \times 10^{15}$
1-0 O(3)	2.8025	6149.2	4.23×10^{-7}	01	6.17×10^{-3}	388.0	0.77	5.27×10^{17}
				02	5.20×10^{-3}	287.0	0.77	4.44×10^{17}
2-1 O(2)	2.7862	11 635.2	1.29×10^{-6}	01	1.11×10^{-4}	6.5	0.75	3.04×10^{15}
3-2 Q(5)	2.7692	19 092.2	3.98×10^{-7}	01	9.81×10^{-5}	5.9	0.74	8.52×10^{15}
3-2 Q(3)	2.7312	17 811.7	4.41×10^{-7}	01	$< 6.55 \times 10^{-5}$	< 3	0.71	$< 4.94 \times 10^{15}$
1-0 Q(13)	2.7269	18 977.1	1.61×10^{-7}	01	1.10×10^{-4}	3.3	0.71	2.27×10^{16}
3-2 Q(2)	2.7186	17 394.5	4.84×10^{-7}	01	$< 2.63 \times 10^{-4}$	< 8.4	0.71	$< 1.79 \times 10^{16}$
2-1 Q(9)	2.7200	18 099.5	3.03×10^{-7}	01	$< 2.63 \times 10^{-4}$	< 8.4	0.71	$< 2.87 \times 10^{16}$
3-2 Q(1)	2.7102	17 092.3	6.86×10^{-7}	01	$< 5.43 \times 10^{-5}$	< 3	0.70	$< 2.60 \times 10^{15}$
2-1 Q(8)	2.6850	16 876.5	3.22×10^{-7}	01	$< 5.29 \times 10^{-5}$	< 3	0.70	$< 5.32 \times 10^{15}$
2-1 Q(7)	2.6538	15 768.7	3.40×10^{-7}	01	3.32×10^{-4}	10.3	0.70	3.13×10^{16}
1-0 Q(11)	2.6350	15 725.5	1.87×10^{-7}	01	3.10×10^{-4}	9.8	0.70	5.29×10^{16}
				02	1.86×10^{-4}	5.6	0.70	3.17×10^{16}
2-1 Q(5)	2.6040	13 889.7	3.74×10^{-7}	01	6.54×10^{-4}	17.2	0.71	5.55×10^{16}
				02	3.58×10^{-4}	40.5	0.71	3.04×10^{16}
1-0 Q(10)	2.5954	14 220.6	1.99×10^{-7}	01	1.55×10^{-4}	9.1	0.72	2.47×10^{16}
				02	1.59×10^{-4}	9.3	0.72	2.53×10^{16}
2-1 Q(4)	2.5850	13 150.2	2.65×10^{-7}	01	1.60×10^{-4}	7.8	0.72	1.91×10^{16}
2-1 Q(3)	2.5698	12 550.2	4.12×10^{-7}	01	4.42×10^{-4}	13.8	0.72	3.40×10^{16}
1-0 Q(9)	2.5600	12 816.4	2.12×10^{-7}	01	$< 8.27 \times 10^{-4}$	< 4.8	0.73	$< 1.24 \times 10^{17}$
				02	$< 7.85 \times 10^{-4}$	< 59.5	0.73	$< 1.17 \times 10^{17}$
2-1 Q(2)	2.5585	12 094.1	4.50×10^{-7}	01	$< 8.27 \times 10^{-4}$	< 4.8	0.73	$< 5.82 \times 10^{16}$
				02	$< 7.85 \times 10^{-4}$	< 59.5	0.73	$< 5.53 \times 10^{16}$
2-1 Q(1)	2.5510	11 789.1	6.37×10^{-7}	01	4.62×10^{-4}	19.2	0.73	2.30×10^{16}
				02	4.25×10^{-4}	43.4	0.73	2.11×10^{16}
4-3 S(1)	2.5415	22 761.0	4.49×10^{-7}	02	6.98×10^{-5}	4.5	0.74	4.93×10^{15}
1-0 Q(8)[h]	2.5278	11 521.5	2.23×10^{-7}	01	3.28×10^{-4}	10.1	0.74	4.66×10^{16}
				02	3.30×10^{-4}	23.3	0.74	4.69×10^{16}
1-0 Q(7)	2.5001	10 340.3	2.34×10^{-7}	01	1.76×10^{-3}	95.2	0.76	2.38×10^{17}
1-0 Q(6)	2.4755	9285.7	2.45×10^{-7}	01	8.49×10^{-4}	29.9	0.77	1.10×10^{17}

Table 3. -Continued

line	λ [μm]	E_u/k [a] [K]	A [b] [s^{-1}]	SWS AOT	I_{obs} [c] [erg $s^{-1}cm^{-2}sr^{-1}$]	S/N[d]	A_λ [e] [mag]	N_u [f] [cm^{-2}]
1-0 Q(5)	2.4548	8364.9	2.55×10^{-7}	01	3.68×10^{-3}	209.0	0.78	4.60×10^{17}
1-0 Q(4)	2.4375	7583.7	2.65×10^{-7}	01	1.61×10^{-3}	76.9	0.79	1.94×10^{17}
1-0 Q(3)	2.4237	6950.6	2.78×10^{-7}	01	5.52×10^{-3}	176.0	0.80	6.34×10^{17}
1-0 Q(2)	2.4134	6471.5	3.03×10^{-7}	01	1.91×10^{-3}	56.3	0.80	2.01×10^{17}
1-0 Q(1)	2.4066	6149.2	4.29×10^{-7}	01	6.31×10^{-3}	195.0	0.81	4.71×10^{17}

[a] The upper level energies were kindly provided by Roueff (1992, private communication).
[b] The Einstein coefficients are taken from Turner et al. (1977) and Wolniewicz et al. (1998).
[c] The upper limit for the intensities is calculated from the 3σ flux density noise level at the respective wavelength, times the width of one resolution element. In a few cases of merged lines it was not possible to derive the individual line intensities. There the measured intensity of the combined structure – although the S/N ratio is > 3 – is also indicated as an upper limit for each of the components.
[d] Calculated from the RMS noise within $\sim 500\,km\,s^{-1}$.
[e] From the extinction curve shown in Fig. 6, derived from the H_2 lines.
[f] Extinction-corrected upper level column density.
[g] The 1-1 S(9) and 0-0 S(9) lines are merged with CO lines. To derive the H_2 line intensities, the CO lines and the background were fit by sine functions plus a first order polynomial, whereas the H_2 lines were fit by a Gaussian.
[h] The 1-0 Q(8) line is merged with H 16-5 line. The respective intensities were derived by fitting two gaussian functions to the combined structure.

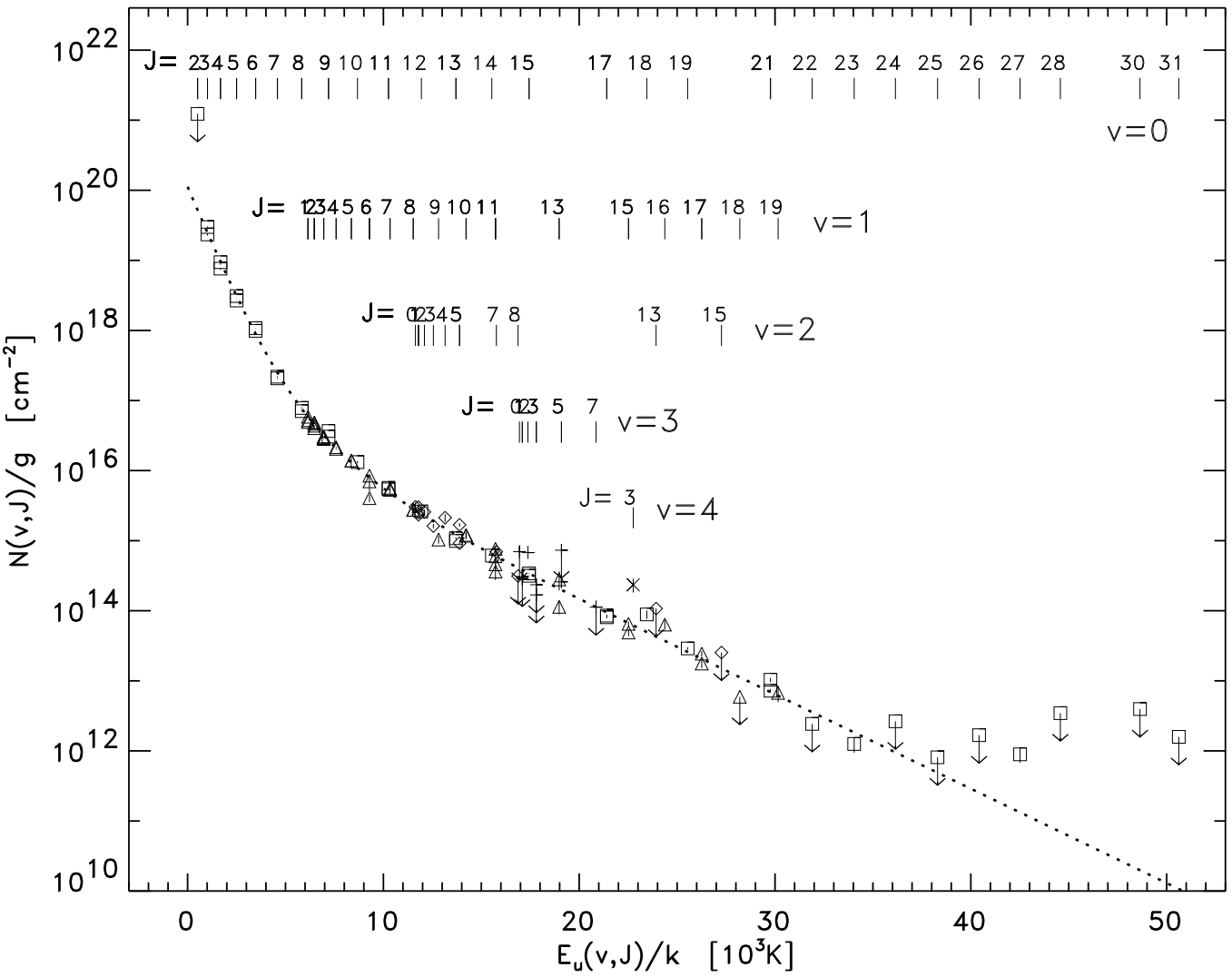

Fig. 8. Extinction-corrected, observed H_2 level column densities, divided by their degeneracy, plotted against the upper level energy $E(v, J)$. Vibrational levels are distinguished by different symbols: squares, triangles, diamonds, +, and × represent $v = 0$, 1, 2, 3, and 4, respectively. The dotted line represents the fit Eq. 5. Error bars represent 1σ flux uncertainties of the line flux integrations, but do not include ∼30% calibration uncertainties. Some lines were measured in two different AOTs, with the corresponding column densities both shown.